

1           A Physics-Based Approach to Modeling Grassland Fires

2           William Mell<sup>A</sup>, Mary Ann Jenkins<sup>B</sup>, Jim Gould<sup>C,D</sup>, Phil Cheney<sup>C</sup>

<sup>A</sup>Building and Fire Research Laboratory, National Institute of Standards and Technology, Gaithersburg, MD USA

<sup>B</sup>Department of Earth & Space Science & Engineering, York University, Toronto, ON M3J 1P3, Canada

<sup>C</sup>Ensis-Forest Biosecurity and Protection, CSIRO, Kingston, ACT, Australia

<sup>D</sup>Bushfire Cooperative Research Centre, East Melbourne, Victoria, Australia

3           May 26, 2006

4           **Abstract**

5           Physics-based coupled fire-atmosphere models are based on approximations to the governing  
6           equations of fluid dynamics, combustion, and the thermal degradation of solid fuel. They require  
7           significantly more computational resources than the most commonly used fire spread models,  
8           which are semi-empirical or empirical. However, there are a number of fire behavior problems,  
9           of increasing relevance, that are outside the scope of empirical and semi-empirical models.  
10          Examples are wildland-urban interface fires, assessing how well fuel treatments work to reduce  
11          the intensity of wildland fires, and investigating the mechanisms and conditions underlying  
12          blow-up fires and fire spread through heterogeneous fuels. These problems are not amenable to  
13          repeatable full scale field studies. Suitably validated coupled atmosphere-fire models are one way  
14          to address these problems. This paper describes the development of a three-dimensional, fully-  
15          transient, physics based, computer simulation approach for modelling fire spread through surface  
16          fuels. Grassland fires were simulated and compared to findings from Australian experiments.  
17          Predictions of the head fire spread rate for a range of ambient wind speeds and ignition line-fire  
18          lengths compared favorably to experiments. In addition, two specific experimental cases were  
19          simulated in order to evaluate how well the model predicts the development of the entire fire  
20          perimeter.

21          Running head: Physics-based grassland fire model

22          Extra keywords: CFD, fire spread, wildland fire, numerical simulation

23          Under review at the *International Journal of Wildland Fire Manuscript # WF06002*

24  
25          Corresponding author:

26          William Mell

27          Building and Fire Research Laboratory, National Institute of Standards and Technology

28          100 Bureau Drive, Stop 8663, Gaithersburg, MD 20899-8663 USA

29          ruddy@nist.gov; (201)975-4797; (301)975-4052 (fax)

## 30 1 Introduction and Background

31 Wildfires and wildland-urban interface (WUI) fires are driven by complex physical and chemical  
32 processes, operating on vastly different scales, whose interactions depend on coupling between the  
33 atmosphere, topography, fire, and solid fuels. Both wildland and WUI fires are very difficult, if  
34 not impossible, to study with full-scale repeatable experiments in the field due to their expense,  
35 safety implications, and variations in atmosphere, terrain, and fuel conditions. Yet, there has been  
36 a long standing need to improve our understanding of these fires (Williams 1982). Forests are  
37 strongly connected to the wildfire regime, and their nature is dependent on the frequency, extent,  
38 and severity of forest fires. Reconciling the need to protect forest lands that are valuable for  
39 industry and recreation with the natural role of fire in maintaining forest ecosystems is a priority  
40 in developing fire management in Canada. Both fire occurrence and average annual area burned  
41 by Canadian forest fires have increased over the past three decades. The records indicate 6,000  
42 fires per year in the 1930 to 1960 period to almost 10,000 fires per year during the 1980s and 1990  
43 (Murphy et al. 2000), where the change in fire occurrence is attributed to a growing population,  
44 expanded forest use, and an increased detection capability (Stock and Simard 1993).

45 Studies in the United States (Appicello 1996) suggest that as a consequence of the past wildfire  
46 management practice of total suppression, many of America's forests have accumulations of historic  
47 dense, dead fallen vegetation. It is maintained that this has made forests more dangerous from  
48 a fire safety perspective and weakened ecologically; fires ignite more quickly, burn with greater  
49 intensity, and spread more rapidly than in the past. According to the US General Accountability  
50 Office, in the 1990s the number and size of wildfires, and the associated fire fighting cost, has  
51 increased dramatically (GAO 1999). In the United States forest fires are an increasing threat to  
52 lives and property. The number of homes at risk of fire in the wildland-urban interface (WUI)  
53 are also likely to increase due to the growing number of people moving into fire-prone areas (GAO  
54 2005). Based on 2000 census information 36% of homes in the United States are within the WUI  
55 (Stewart et al. 2003). In California alone, homes in the WUI account for 42% of the total homes.  
56 Wildland fires in Southern California spreading through WUI areas in 2003 resulted in \$2 billion  
57 of estimated insured losses (GAO 2005). Homes at risk to WUI fires are also located in Arizona,  
58 Colorado, Georgia, New Mexico, New York and Florida (Zicherman 2004).

59 The most commonly used operational models for wildland fire spread rely on empirically derived  
60 relations to predict the spread rate of a fire and quantities derived from the spread rate. Examples  
61 of such models are BehavePlus (Andrews et al. 2003) and FARSITE (Finney 1998) in the United  
62 States, the Forest Service Fire Behavior Prediction System (Hirsch 1996) in Canada, and the Mk 4  
63 MacArthur Fire Danger Meters (Nobel et al. 1980), and the CSIRO Grassland Fire Spread Meter  
64 in Australia. The essence of these models is that the local fire spread rate is prescribed as a  
65 function of wind speed, terrain slope, humidity, and fuel characteristics. No account is taken,  
66 except for tuning the coefficients, for the fire/fuel and fire/atmosphere interactions. The data used  
67 to derive the empirical correlations employed in these models were taken either directly from field  
68 experiments/observations (Hirsch 1996; Nobel et al. 1980) or from laboratory scale experiments  
69 with a flat flame front with a quasi-steady spread rate across spatially homogeneous surface fuels  
70 on flat beds without a wind (Rothermel 1972; Albini 1976). Spread rates used in BehavePlus  
71 and FARSITE are based on semi-empirical relations developed by Rothermel (1972). Such models  
72 provide fire spread predictions quickly and can be easily applied to conditions that are outside those  
73 in the laboratory, sometimes with non-physical results (Beer 1991). They are also unable to predict  
74 fire behavior in the intermix of vegetative and structural fuels that comprise the wildland-urban  
75 interface.

76 As discussed by Finney (1998) FARSITE is unable to predict the transient behavior of a fire due

77 to changes in the local environment induced by the fire itself (e.g., fire/atmosphere interaction).  
78 This is because the fire shape, size and spread rate are assumed constant for a given fuel, wind, and  
79 slope. The prediction of local wind and the interaction of the fire and wind is of major importance  
80 to predicting fire behavior, especially severe, fire behavior Albini (1993). Fires where strong fire-  
81 atmosphere interactions occur, such as crown fires, routinely strain the credibility of the empirical  
82 fire spread models.

83 Development of these models began in the 1970s. At that time computational resources and  
84 numerical methods were not sufficiently advanced to allow three-dimensional time dependent sim-  
85 ulations of wildland fires. With the dramatic increase in the capability of computers and numerical  
86 approaches in the last 30 years, population growth in wildland-urban interface areas, and the in-  
87 creased role of prescribed burns in forest management, there is an opportunity and a need for more  
88 capable physics-based fire models. Suitably validated physics-based models for wildland and WUI  
89 fires, which predict both fire spread and smoke transport, have a number of applications:

- 90 • evaluate operational models over a wide range of relevant conditions,
- 91 • provide more realistic sources of heat and smoke for the new generation of regional smoke
- 92 transport models operating on present day computational platforms (e.g., BlueSky (2004)),
- 93 • help land and smoke managers plan and evaluate prescribed burns,
- 94 • assess the effects of fire on vegetation during prescribed burns,
- 95 • assess how fuel treatments influence fire spread and the resulting fire effects on vegetation,
- 96 • provide a means by which established communities or homeowners can assess and/or reduce
- 97 their risk to WUI fires,
- 98 • help plan firewise communities by both reducing the risk from fire spread and planning smoke
- 99 free evacuation routes,
- 100 • deliver predictions of fire spread and smoke transport to incident managers to aid their man-  
101 agement of fire fighting and evacuation logistics.

102 In general, simulations of wildfires require models for both the fire/fuel interaction and the  
103 fire/atmosphere interaction. The fire/fuel interaction involves gas generation by solid fuel pyrolysis,  
104 the subsequent combustion of the fuel gases, and the resulting heat flux back to the solid fuel, driving  
105 continued pyrolysis and fire spread. The fire/atmosphere interaction involves the response of both  
106 the fire and its plume to the ambient winds, and the response of the atmosphere to the buoyant fire  
107 plume. The fire/atmosphere interaction can alter the orientation and geometry of the fire plume,  
108 influencing the distribution and intensity of the net heat flux to the solid fuel, and the downwind  
109 transport of firebrands and smoke. At larger spatial and temporal scales, the interaction of the fire  
110 plume with the atmosphere can result in macroscopic (on the scale of the fire front) atmospheric  
111 processes such as pyrocumulus formation. At even larger scales, diurnal cycles in humidity and  
112 temperature, and synoptic weather patterns, can influence the behavior of the fire and its smoke  
113 plume.

114 Figure 1 is a schematic showing the atmosphere, fire, and vegetative fuel components of wildland  
115 fire models at the corners of a triangle. Different fire models are located on the figure according to  
116 the emphasis they place on each of these three components and their interaction. The Canadian  
117 FBPS (Hirsch 1996), the Australian McArthur meters (Nobel et al. 1980), and the US FARSITE  
118 (Finney 1998) and BEHAVE (Andrews 1986; Andrews et al. 2003) are all located in region V  
119 since these empirical or semi-empirical, not physics-based, fire models and they require only inputs  
120 describing the vegetative fuel, terrain, and wind.

121 The focus of this paper is on modeling solid fuel pyrolysis, heat transfer, gas phase combustion  
122 (i.e., the fire/fuel interaction) and local fire/atmosphere interaction. A fuller investigation of large-  
123 scale fire/atmosphere interactions described above, along with firebrand generation and transport,

124 will be considered later. In this paper the overall modeling approach is broken into two components:  
125 1) the pyrolysis of vegetative fuels and, 2) gas phase combustion. Models for each are implemented  
126 within the Fire Dynamics Simulator (FDS) developed at the Building and Fire Research Laboratory  
127 at the National Institute of Standards and Technology (NIST) (McGrattan 2004) over the last 30  
128 years. FDS numerically solves a form of the Navier-Stokes equations appropriate for low-speed,  
129 thermally-driven flow with an emphasis on smoke and heat transport from fires. It is aimed at  
130 solving practical fire protection engineering problems (i.e., fires in structures) while providing a tool  
131 to study fundamental fire dynamics and combustion. Simulations can be run on single or multiple  
132 processors on most modern computer platforms. The version of FDS used here is extended to  
133 include fire spread in vegetative fuels and is referred to as WFDS (WUI Fire Dynamics Simulator).

134 In this paper the development of the current version of WFDS is described and evaluated by  
135 comparing its predictions of fire behavior to open grassland fire experiments conducted by CSIRO  
136 in Australia (Cheney et al. 1993; Cheney and Gould 1995). The relatively simple scenario of  
137 grassland surface fires provides an appropriate first step to evaluating WFDS since the fuels are to  
138 a good approximation thermally thin, spatially homogeneous, occur on flat terrain, and fire spread  
139 is mostly restricted to horizontal directions (i.e., there is relatively little upward fire spread as can  
140 occur in suspended vegetation such as large tree crowns).

## 141 2 Review of physics-based wildland fire models

142 Fire models can be classified into three types (Pastor et al. 2003): empirical, semi-empirical, or  
143 theoretical. Empirical models involve no physics-based modeling since they are derived from sta-  
144 tistical correlations of a given experimental data set. Semi-empirical models are based on energy  
145 conservation but do not distinguish between the different modes of heat transfer (conductive, con-  
146 vective, radiative). Theoretical models attempt to solve (in some approximation) the equations  
147 governing fluid dynamics, combustion, and heat transfer. Here we refer to theoretical models as  
148 physics-based models since the physical processes governing the hydrodynamics, combustion, and  
149 energy transfer are modeled. Vegetative fuels and fires in a wildland setting are categorized as  
150 ground, surface, or crown types (e.g., Chap. 4 in Johnson and Miyanishi (2001)). Examples of  
151 fuels in surface fires include fallen twigs, leaves, bark, branches, grasses, and shrubs less than 1.8  
152 m tall (Davis 1959).

153 As discussed in the previous section, a complete physics-based wildland fire simulation would  
154 include models of the fire/atmosphere and the fire/fuel interactions. In this section a short overview  
155 of existing physics-based models that can be applied to surface fires is given. Figure 1 is used to  
156 order the discussion. Note that some approaches are formulated to include a wide range of physics  
157 but then implemented in a simpler, reduced, form. This is true of the approach formulated by Sero-  
158 Guillaume and Margeri (2002), and then implemented by Margeri and Sero-Guillaume (2002). Such  
159 cases are placed on Fig. 1 based on the version of the model that was implemented.

160 Over the last 60 years, starting with Fons (1946), many physics-based fire/fuel models for a fire  
161 spreading along a spatially homogeneous fuel bed have been presented. Examples are Albini (1985);  
162 De Mestre et al. (1989); Margeri and Sero-Guillaume (2002). Weber (1991) provides an excellent  
163 review of these (and other) models up to circa 1989. In these approaches the fire/atmosphere  
164 interaction is not modeled. Relevant flame properties, such as the temperature and flame geometry,  
165 and therefore the heat flux from the fire, are fixed. This removes the need for modeling the fire in  
166 the fire/fuel interaction. While these models have slope and wind inputs, their physical modeling is  
167 focused on heat transfer within the fuel. For this reason they are designated ‘fuel driven’ models on  
168 Fig. 1 and located in Region I where modeling of the fire and atmosphere physics is less emphasized.

169 The basis of most of these models is that the steady flame spread rate is determined by how long  
170 it takes the solid fuel ahead of the flame to reach an ignition temperature at an idealized two-  
171 dimensional ignition interface. Such models are useful for exploring the relative contributions of  
172 the different modes of heat transfer but only for conditions appropriate for steady flame spread  
173 where net wind speed and direction, fuel properties, terrain, etc., are all constant.

174 More recently, multidimensional, transient, wildfire simulation approaches that use the methods  
175 of computational fluid dynamics to include the fire/atmosphere interaction, to varying degrees of  
176 complexity, have been developed. These methods are grouped in regions II, III, and IV.

177 Region II has been labelled ‘multiphase’ models by most of the authors using this approach which  
178 was first presented by Larini et al. (1998) and subsequently used by Porterie et al. (2000), Zhou and  
179 Pereira (2000), Morvan and Dupuy (2001), Morvan et al. (2002a), Morvan et al. (2002b), Morvan and  
180 Dupuy (2004) and Dupuy and Morvan (2005) for flame spread through forest fuels. These models  
181 will be denoted MM, for multiphase models, in the following text. While the formulation of the  
182 MM is three-dimensional to date all MM studies have been implemented on two-dimensional grids.  
183 The largest reported computational domain size is 200 m wide and 50 m high; 200 s of simulated  
184 time required between 12 to 48 cpu hours on a single (2 GHz) processor (Dupuy and Morvan 2005).  
185 Since the MM results have been, to date, two-dimensional the complete fire/atmosphere interaction  
186 was not captured. For this reason they are placed along the vegetative fuel/fire boundary in Fig. 1.  
187 However, two-dimensionality allows relatively fine computational grids to be used and, therefore,  
188 more complete models for the thermal degradation of the vegetative fuel, the subsequent combustion  
189 of pyrolysis vapors, and the local two-dimensional fire/atmosphere interaction. The computational  
190 cost due to the complexity of the physical models limits the application of the approach to medium-  
191 scale line fires (Morvan and Dupuy 2004).

192 Characteristic of the MM in region II is that of Morvan and Dupuy (2004). They model fire  
193 spread through a vegetation complex consisting of thermally-thin shrubs, twigs, and grass. The  
194 solid fuel is approximated as a set of fixed fuel elements. The thermal (convective heat flux) and  
195 drag interaction of the solid fuel with the gaseous flow is accounted for by using coefficients from  
196 empirical correlations for representative shapes (cylinders, spheres, etc.). Moisture evaporation and  
197 pyrolysis are modeled with simplified temperature dependent mass loss rates. Arrhenius kinetics  
198 are used for char oxidation. Gas phase combustion kinetics are assumed to be infinitely fast and  
199 the eddy dissipation model is used to determine gas-phase reaction rates. Thermal radiation in a  
200 multiphase medium (where the volume fraction of solid vs. gas is accounted for) is solved with a  
201 Discrete Ordinates solver that accounts for thermal radiation transfer within the vegetation fuel  
202 complex. An evolution equation for the soot volume fraction is solved, and a re-normalization  
203 group (RNG)  $k-\epsilon$  turbulence model is used. Minimum grid resolutions in the fuel bed were  $\Delta x =$   
204  $0.1 \text{ m}$ ,  $\Delta z = 0.03 \text{ m}$ .

205 Region II also includes the simulations of Grishin and collaborators (e.g., Grishin et al. (1985);  
206 Grishin (1996)). The formulation of the model equations is very general, including solid pyrol-  
207 ysis, gas phase chemistry, and thermal radiation. However, it is unclear how these models are  
208 implemented and whether or not the reported simulation results, which span a 23 m long by 15  
209 m high domain, are two or three dimensional (Grishin 1996). A  $k - \epsilon$  turbulence model and P1  
210 approximation for thermal radiation were used.

211 The methods in region III include those developed by Costa et al. (1995), Clark et al. (1996),  
212 Coen (2003), and Clark et al. (2003, 2004), all of which obtain the heat and moisture release, fuel  
213 consumption, and fire spread rate from either a prescribed formula or semi-empirical relations. For  
214 this reason, computational resources can be devoted to resolving atmospheric physics. For example,  
215 in the approach of Clark and colleagues (which is denoted by NCAR on Fig. 1 since its development  
216 began at the National Center for Atmospheric Research in the U.S.), a time dependent three-

dimensional, non-hydrostatic, cloud-resolving numerical prediction model for the atmosphere is used. The cloud-resolving model can include vertically-stretched and terrain-following coordinates, and multilevel grid nesting. A recently reported application of this approach is Coen (2005). Fire spread rates are obtained from the semi-empirical Rothermel (1972) formulas. Sensible and latent heats from the fire are distributed vertically with an exponential decay over an assumed height. These approaches provide a first approximation to the fire/atmosphere coupling, especially suitable to large scale simulations on coarse grids (from a combustion physics point of view). On Fig. 1 BlueSky refers to the modeling framework developed by the US Forest Service for smoke transport from forest, agricultural, and range fires across regional scales (BlueSky 2004).

Region IV includes three-dimensional simulations that have physics-based models for the vegetative fuel, the atmosphere, and the fire. Linn and colleagues have developed a model called FIRETEC (Linn 1997; Linn et al. 2002; Linn and Cunningham 2005). FIRETEC was designed to operate over landscape scales (100s of meters) of flat or complex terrain. The three-dimensional nature of the model and its focus on the coupling between the atmosphere and fire constrain the ability of this model to use far sub-meter resolution over domains more than 300 m in all directions (Linn 2005). Thus, the fine-scale turbulence and combustion processes can not be resolved directly and must be approximated with subgrid models. In fact, any three dimensional simulation, run on present day computational platforms, of full scale fires requires subgrid models (including WFDS).

The governing model equations in FIRETEC are based on ensemble averaging, in a manner similar to Reynolds averaging, of the conservation equations for mass, momentum, energy, and chemical species. This results in additional closure equations which require a number of turbulence modeling assumptions. FIRETEC is coupled to an atmospheric model HIGRAD (Reisner et al. 2000). The numerical time stepping scheme explicitly handles the high frequency acoustic waves. Thermal radiation transfer is computed using a diffusional transport approximation adapted from Stephens (1984). The chemical heat release from combustion occurs only in computational grid cells that contain the solid fuel (Linn et al. 2002). For grid cell dimensions that are smaller than the flame length this is unrealistic and improvements are underway (Colman and Linn 2003, 2005). A rate of heat release is determined from a universal reaction rate that is a function of the density of both the solid fuel and the gas phase, and an assumed Gaussian-shaped probability density function (PDF) of the temperature within a grid cell. The use of this PDF is physically motivated by the assumption that in general there are wide variations in temperature within a grid cell which are not sufficiently represented by the resolved temperature. The heat release rate, determined from the universal reaction rate and a heat of combustion of the volatiles, is partitioned between the gas and the solid (Linn et al. 2002). In both the gas and the solid phase energy equations these terms are exothermic. A weight factor is applied to these exothermic terms. In the solid phase energy equation the weight factor increases as the solid burns away; in the gas phase energy equation the weight factor has the opposite trend. For example, the weight factor that determines how much energy is returned to the solid fuel ranges from 25% to 75%; the highest value is applied when oxygen is abundant and more than 60% of the solid fuel mass is gone (Linn 2005). The motivation for this approach is to account for the progression from flaming to non-flaming combustion and to model the unresolved subgrid heat transfer processes in the vicinity of the fire.

Compared to the MM approach (which more directly solves the governing equations on more highly resolved two-dimensional computational grids) FIRETEC currently relies more on heuristic, physically-motivated assumptions, such as a prescribed subgrid probability distribution of the temperature in a grid cell and a rule for partitioning the energy release rate into the gas and solid phase equations. Many of these assumptions are driven by the limitations on spatial resolution in FIRETEC.

### 264 3 Overview of WFDS modeling approach

265 This section is an overview of the WFDS modeling approach. A detailed description of the model  
266 equations for the gas phase and vegetative fuel is given in Appendix A. The approach is similar to  
267 the MM approach described above (e.g., Porterie et al. (1998)) because separate but coupled models  
268 for the thermal degradation of the solid fuel and gas phase combustion are employed. This allows  
269 for a straightforward use of some of the physics-based solid phase models in region I of Fig. 1. As  
270 discussed above, these fuel driven models use an assumed flame geometry and temperature. Thus,  
271 in place of a constant heat flux on the solid fuel from an assumed flame, a transient heat flux (both  
272 convective and radiative) is used. This heat flux results from the local fire/atmosphere interaction  
273 as determined by the numerical solution of the conservation equations for momentum, total mass,  
274 energy, and the major species. Combustion is modeled with a mixture fraction based approach.

275 Unlike the MM approach, which is limited to two dimensional grids, WFDS can simulate fires in  
276 two or three dimensions (only fully three-dimensional simulations, with no symmetry assumptions,  
277 are reported here). Since three-dimensional simulations require significantly more computational  
278 resources, WFDS grids are coarser than those used in the MM approach. As a result, a combus-  
279 tion modeling approach appropriate for computational grids that significantly under-resolve the  
280 combustion zone must be used. The approach used here is described in Appendix A. Compared  
281 to FIRETEC, which also operates on coarse grids (relative to the MM approach), WFDS more  
282 directly solves the equations governing the interaction of the fire/fuel and fire/atmosphere, relying  
283 less on heuristic physically motivated assumptions to include physical processes. For example, the  
284 thermal degradation of the solid fuel is driven solely by the resolved net heat flux on the fuel.  
285 In FIRETEC an additional amount of energy, a fraction of heat released by a combined solid-gas  
286 reaction, is deposited in the solid fuel (Linn and Cunningham 2005).

287 The basis of the surface vegetation model in WFDS is the physical assumption that combustion  
288 (i.e., heat release) occurs predominantly above the surface fuel bed. This is consistent with flame  
289 heights above the fuel bed that are significantly larger than the height of the fuel bed itself. With  
290 this assumption, two computational grids can be used: one for the gas phase that resolves the fire  
291 plume and another for the vegetative fuel bed that resolves heat transfer and thermal degradation.  
292 The fire plume can be resolved on a much coarser grid than the thermal degradation of the veg-  
293 etation. The equations solved and numerical method employed in the gas phase calculation are  
294 essentially those used by FDS McGrattan (2004); details are in the appendix. The vegetation is  
295 “seen” by the gas phase as a source of momentum drag and heat and mass fluxes along the bottom  
296 boundary of the gas phase. Heat flux from the fire and the flux of fuel gas (from pyrolysis) both  
297 occur along the upper boundary of the grid for the vegetative fuel bed. A method that is similar  
298 to the multiphase approach discussed previously is then used to model the evolution of solid phase.  
299 Gas phase temperatures in the fuel bed are obtained from the gas phase computational grid directly  
300 above. The approach is described in more detail in the appendix. Note that this approach is less  
301 valid for vegetative fuels through which significant vertical flame spread and air flow can occur  
302 (such as through tree crowns). For the Australian grassland fire experiments simulated here the  
303 observed flame heights above the fuel bed were approximately 4 times the height of the fuel bed.

304 Figure 2 shows the time history of a number of solid phase quantities, in the uppermost layer of  
305 the solid fuel model, for two different wind speeds: in Fig. 2(a)  $U_2 = 1 \text{ m s}^{-1}$  and in Fig. 2(b)  
306  $U_2 = 5 \text{ m s}^{-1}$ . The grassland fuel properties measured in experiment F19 conducted in Australia  
307 were used (see Table 1; details of this experiment are given in Sec. 4.6). The time interval in each  
308 plot is 15 s. In the slower wind case, Fig. 2(a), 15 s is the time required for evaporation of the  
309 fuel moisture ( $T_s = 100 \text{ C}$ ) and the subsequent pyrolysis of the solid fuel (leaving only char). At  
310 this point in the model development char oxidation (smoldering combustion) is not accounted for.

311 In Fig. 2(b) boiling and pyrolysis occur over a shorter time interval of 4 s, due to the higher heat  
312 fluxes on the solid fuel. The peak heat fluxes are over a factor of two larger in the higher wind  
313 case. The higher wind forces both the flame and the hot fire plume closer to the downwind fuel bed  
314 (see Fig. 5), increasing both the radiative and convective heat fluxes. This is a well known process  
315 leading to faster fire spread in stronger winds. For both wind speeds, radiation is the dominant heat  
316 transfer mechanism. In the simulations of Morvan and Dupuy (2004) the relevance of convective  
317 heat transfer was found to increase with increasing wind speed, eventually becoming the dominant  
318 mode of heat transfer. Their two-dimensional simulations use significantly smaller gas-phase grid  
319 cells ( $\mathcal{O}(10)$  cm compared to  $\mathcal{O}(1)$  m) resulting in much higher, and more realistic, gas phase  
320 temperatures in the fire plume. As a result, convective heat transfer into the solid fuel in regions  
321 of active combustion are underestimated in WFDS. This is an area of further model development.  
322 However, as will be seen below, WFDS does reproduce many experimentally observed fire spread  
323 trends.

## 324 4 Results

### 325 4.1 Overview of grassland fire experiments

326 Experiments were conducted on a 2500 ha (25,000,000 m<sup>2</sup>) site in the Northern Territory of Aus-  
327 tralia, during July and August 1986 (Cheney et al. 1993; Cheney and Gould 1995). Fuels were  
328 open grasslands, and grasses were continuous, and normally fully cured. The site was divided into  
329 170 plots, that were 100 m x 100 m, 200 m x 200 m, or 200 m x 300 m in size. A total of 121 of  
330 these grassland fires was used by Cheney et al. (1993) to examine the influence of fuel and wind on  
331 the spread rate of the head fire,  $R$ . Each fire travelled over flat terrain.

332 Plots contained one of two distinct grass types: *Eriachne burkittii* (kerosene grass), a coarser  
333 grass, with a mean surface-area-to-volume ratio of 9770 m<sup>-1</sup>; and *Themeda australis* (kangaroo  
334 grass), a finer grass, with a mean surface-area-to-volume ratio of 12240 m<sup>-1</sup>. Selected plots were  
335 harvested to alter the height  $h_s$  (m), load  $w_s$  (kg m<sup>-2</sup>), and bulk density  $\rho_{sb}$  (kg m<sup>-3</sup>) of the fuel.  
336 Plots were either natural or cut at 25 to 50 percent of natural grass height. The cut fuels either  
337 remained or were removed. A characteristic  $h_s$ ,  $w_s$ , and  $\rho_{sb}$  were determined for each plot, and  
338 only plots with fairly even fuel load and continuous fuels were included in the analysis. Moisture  
339 content of the grass fuel,  $M$ , as a fraction of the oven dried weight of the grass was measured.

340 Wind speeds at 2 m AGL (Above Ground Level) were measured in the open area immediately  
341 upwind and within 800 m of each fire. Wind speeds at 2 m AGL at each corner of the experimental  
342 plot were also measured at 5 s intervals for the duration of the fire. Wind orientation was not  
343 measured, only the speed of the horizontal wind. Ignition by field workers carrying drip torches  
344 started at the mid-point of a measured line and moved rapidly toward each end along the upwind  
345 edge of the grass plot. Thus, the fire could not spread upwind. Ignition lines were nominally 50  
346 m long on 100 m x 100 m plots, and up to 175 m long on the larger plots. Ignition line fires were  
347 oriented at right angles to the prevailing wind direction. The average forward rate of spread  $R$  (m  
348 s<sup>-1</sup>) was determined over the longest period of spread before a substantial change in the rate of  
349 spread.

### 350 4.2 Overview of the numerical simulations

351 A number of simulations, with ignition line-fires of varying length ( $L_{ig}$ ), depth ( $d_{ig}$ ), and wind  
352 speed 2 m above the ground ( $U_2$ ) were conducted to assess how well WFDS predicts the spread  
353 rate of the head fire. Two additional simulations, of specific Australian grassland experiments (F18

354 and C064, in Table 1), were run to evaluate WFDS predictions of the behavior of the entire fire  
355 perimeter.

356 The physical parameters required by the model are listed in Table 1 for both the gas phase and  
357 the vegetative fuel. Whenever possible, values obtained from the grass fire experiments are used.  
358 Properties that were not measured in the field were determined from literature sources for similar  
359 conditions (see Table 1). All boundaries except the inflow and bottom are open. At the open  
360 boundaries the density and mixture fraction have zero gradient conditions; velocity and pressure  
361 boundary conditions are described in McGrattan (2004).

Initially, throughout the domain and at the inflow boundary for the duration of the simulation, the dependence of the ambient wind with height above the ground,  $z$ , is defined to follow a power law:

$$U(z) = U_{2,i}(z/2)^{1/7}. \quad (1)$$

362 Here  $U_{2,i}$  is the value in WFDS of the initial wind speed at a height of 2 m. This expression is  
363 suitable for smooth terrain and has been used in simulations of fire spread in pine needle beds  
364 (Morvan and Dupuy 2001) and in a grass/shrub fuel bed (Morvan and Dupuy 2004). Other  
365 ambient wind profiles can easily be implemented but their influence on simulated fire behavior  
366 will be investigated elsewhere (e.g., Mell et al. (2005b)). In general,  $U_2$  can be modified by drag  
367 from surface vegetation and the fire plume (due to both entrainment and blockage effects). When  
368 comparing head fire spread rates from WFDS and the experiments over a range of conditions a  
369 consistent measure of the representative ambient wind speed  $U_2$  must be used. The experimental  
370 value of  $U_2$  was determined by averaging, over the time interval spanning ignition to when the fire  
371 reached the downwind firebreak, the measured horizontal wind speed at the two upwind corners of  
372 the plot (see Fig. 3). The simulated value of  $U_2$  was determined by averaging, over the same time  
373 interval used to compute the experimental  $U_2$ , the horizontal wind speed in the grid cell located at  
374 the center of the ignition line fire and at a height of  $z \approx 2$  m. For the simulations reported here  
375 this velocity was within a height range of  $z = 1.95$  m to 2.1 m. The magnitude of the crosswind  
376 velocity,  $v$ , in WFDS was initially zero and remained much smaller than  $u$  so that  $\sqrt{u^2 + v^2} \approx u$ .  
377 The corner values of the simulated velocity were not used to define  $U_2$  in the simulations because  
378 they were not representative (they were too low due to drag from unburned vegetation) of the wind  
379 speed upwind of the head fire.

380 The heat release rate per unit area of an ignition line fire has two components: the burning grass  
381 and the hydrocarbon fuel deposited by the drip torches. The hydrocarbon fuel was assumed to be  
382 gasoline (heat of combustion 32 MJ L<sup>-1</sup>) deposited with an area density of 0.25 L m<sup>-2</sup>. Complete  
383 burning of the gasoline and grass fuel was assumed to occur over a time interval equal to  $d_{ig}/R_{ig}$   
384 where  $R_{ig} = 0.3$  m s<sup>-1</sup> is assumed (based on experimental head fire spread rates). For example,  
385 in simulations using the grassland fuel present in experiment F19 (see Table 1) an ignition line fire  
386 of depth  $d_{ig} = 3.3$  m had a duration of 11 s and a heat release rate per area of 1460 kJ m<sup>-2</sup>. The  
387 ignition procedure, which can be easily modified, will affect the initial behavior of the fire. Since  
388 the information available for the field ignition method was incomplete (e.g., it is unknown how  
389 much liquid fuel was distributed on the grass) the method used here is a best estimate to the field  
390 procedure.

391 Care must be taken to avoid nonphysical numerical boundary affects. A fire entrains the sur-  
392 rounding ambient air into its rising plume. The numerical boundaries must not interfere with this  
393 process in a significant way. For example, when the inflow boundary (at which the wind speed is  
394 held fixed) is too close to the fire, entrainment from the upwind direction is reduced. This can  
395 have significant effects for sufficiently low ambient wind speeds. In reality, under such conditions

396 entrainment by a fire plume in an unbounded domain can add to the ambient wind oriented into  
397 the head fire. In numerical simulations with upwind boundaries that are too close to the fire, the  
398 flame spread rate increases as the boundary is moved further from the fire.

399 It was found that spread rates and fire behavior were nearly identical when the grassland plot was  
400 centered in a 1500 m versus a 2700 m square domain. In the simulations discussed below, therefore,  
401 the fires occurred within a 300 m by 300 m plot surrounded by a 600 m border on all sides (1500  
402 m by 1500 m area). A number of tests were made to check the influence of grid resolution on head  
403 fire spread rates. In these tests the sizes of horizontal grid cells were  $\Delta x = \Delta y = 1$  m, 1.66 m, or  
404 3.33 m. As the grid resolution increased, the head fire spread rate decreased somewhat. Spread  
405 rates with the  $\Delta x = 1$  m were 15% (or less) slower than the  $\Delta x = 3.33$  m cases and 10% (or  
406 less) slower than  $\Delta x = 1.66$  m cases. Table 2 contains the values for grid resolution and other  
407 parameters for the production simulation runs.

408 Production simulations (1500 m  $\times$  1500 m  $\times$  200 m, in general) required 16 million grid cells  
409 and 11 processors. The total cpu time required for these runs depended on the overall heat release,  
410 which increases with fuel loading. For most of the cases considered 44 cpu hours were needed for 100  
411 s simulated time (i.e., all 11 processors running for 44 hours on 1.8 GHz processors). Exploratory  
412 simulations run much faster, on the order of 2 hours on a single processor. These faster runs were  
413 on smaller domains and provide reasonable results if the ambient wind speed is sufficiently high.  
414 For lower ambient wind speeds ( $\mathcal{O}(1)$  m s $^{-1}$ ) natural entrainment was influenced by the presence  
415 of numerical boundaries as discussed above. Thus, for consistency all simulations had horizontal  
416 domains of 1500 m  $\times$  1500 m.

417 It should be noted that the results of any large scale simulation will depend on both the grid res-  
418 olution and the modeling assumptions employed. Fully resolving the combustion zone (as captured  
419 by the relatively simple fast-chemistry mixture fraction approximation used here) requires sub-  
420 millimeter grid resolution (Mell et al. 1996). The larger scale fire/fuel interactions, which control  
421 the heat transfer to the fire bed, occur on scales on the order of 1 m to 10 m for grass fires, a factor  
422 of over a thousand greater. Fire/atmosphere interactions occur over even larger scales. Present  
423 day computers (even massively parallel platforms containing thousands of processors) do not have  
424 the memory capacity or processor speeds to fully resolve processes occurring from the combustion  
425 zone up to scales that characterize the fire/atmosphere interactions. For this reason, the governing  
426 equations must be approximated in a way that retains the physical processes that are most rele-  
427 vant to the fire problems under study. Here the emphasis is placed on resolving the larger scale  
428 fire plume dynamics and heat transfer processes, in the fire/fuel and fire/atmosphere interactions,  
429 that drive fire spread (as opposed to smaller scale combustion processes of, for example, chemical  
430 kinetics and soot generation). In the following sections WFDS will be evaluated by determining  
431 how well it reproduces observed fire-spread trends in the Australian grassland experiments.

432 A characteristic example of both the experiment and simulation is shown in Fig. 4. A photograph  
433 of the fire perimeter taken during experiment F19 is shown in Fig. 4(a). A rendering of the simulated  
434 fire front and smoke plume using the visualization tool Smokeview (Forney and McGrattan 2004)  
435 is plotted in Fig. 4(b). As discussed above, smoldering combustion is not currently modeled. For  
436 this reason, there is no smoke generated upwind of the fire in the simulation (Fig. 4(b)).

### 437 **4.3 Effect of wind on head fire spread**

438 Cheney et al. (1993) found that when head fire spread rate was correlated with fuel type, wind  
439 speed, and fireshape variables, wind speed  $U_2$  had the most effect on the spread rate. Convective  
440 activity was thought to be a primary factor that determined whether fires progressed steadily in  
441 the direction of the prevailing wind, and fires burning under light wind conditions often spread

442 erratically as they responded to gust and lulls caused by the localized thermal activity. As the  
 443 wind speed increased, the head fire width required for fires to approach their potential quasi-  
 444 steady rate-of-forward spread,  $R_s$ , also increased. Cheney et al. (1993) note that the wind directly  
 445 influencing fire spread is the net wind at the flame zone, not the wind measured remote from the  
 446 fire. However, since this net wind speed is not known and would be very difficult to measure,  
 447 empirical formulas for the spread rate of the head fire are based on a representative ambient wind  
 448  $U_2$ . The determination of  $U_2$  was discussed in Sec. 4.2.

The following empirically based formula (Eq. 4 in Cheney et al. (1998)) relates the experimentally observed head fire spread rate  $R_o$  ( $\text{m s}^{-1}$ ), to the measured wind speed  $U_2$ , the head fire width  $W$  (m), and the fuel moisture content  $M$  (%):

$$R_o = (0.165 + 0.534U_2) \exp(\{-0.859 - 2.036U_2\}/W) \exp(-0.108M). \quad (2)$$

They defined the head fire width,  $W$ , as the width of the fire, measured at right angles to the direction of head spread, which influenced the shape and size of the head fire during the next period of spread measurement (Cheney and Gould 1995). The effective width of the head fire can also be defined as that portion of the perimeter where the flames are leaning towards unburnt fuel. In WFDS the head fire width was defined to be the distance between the flank fires one fire depth upwind of the trailing edge of the head fire (see Fig. 3). With increasing head fire width,  $W \rightarrow \infty$ , the head fire spread rate, Eq. (2), increases and asymptotes to a potential quasi-steady spread rate (Cheney et al. 1998):

$$R_s = (0.165 + 0.534U_2) \exp(-0.108M) \quad (3)$$

449 In the figures to follow, simulated head fire spread rates and head fire location were compared to  
 450 their experimentally observed values through the use of these empirical spread rate relations.

451 Simulations using four different ignition line fires,  $L_{ig} = 8 \text{ m}, 25 \text{ m}, 50 \text{ m}, 100 \text{ m}$ , and four wind  
 452 speeds,  $U_2 = 1 \text{ m s}^{-1}, 3 \text{ m s}^{-1}, 4 \text{ m s}^{-1}, 5 \text{ m s}^{-1}$  (16 simulations in all) were run. See Table 2 for a  
 453 summary of the simulations. For each case the line fire was ignited simultaneously along its entire  
 454 length. The fuel bed parameters of experiment F19 (see Table 1) were used. The wind speeds  
 455 used are such that the fire-atmosphere interaction ranges from a more plume dominated fire to a  
 456 wind dominated fire (Pagni and Peterson 1973; Pitts 1991). Figure 5(a) shows the more plume  
 457 dominated case ( $U_2 = 1 \text{ m s}^{-1}$ ). In this figure the plume rise close to the ground ( $z < 20 \text{ m}$ ) is  
 458 dominated by buoyancy resulting in a nearly vertical rise. In Fig. 5(b) the wind ( $U_2 = 5 \text{ m s}^{-1}$ )  
 459 dominates the plume rise. As shown previously in Fig. 2 the net heat flux to the solid fuel is  
 460 significantly higher for the faster wind speed case due to flame tilt toward the unburned fuel bed.

461 Figure 6 is a plot of head fire spread rate versus wind speed. Spread rates from WFDS (symbols),  
 462 BehavePlus (Andrews et al. 2003) (solid line) and the empirically derived quasi-steady spread rate  
 463 form of Eq. (3) (i.e.,  $W \rightarrow \infty$ ) (dashed line) are shown. The spread rate from WFDS was obtained  
 464 from the time history of the leading edge of the head fire. The leading edge was identified by the  
 465 location of non-zero fuel mass loss rate, along the centerline of the grass plot, that was furthest  
 466 downwind. As will be seen below, in Fig. 7, WFDS spread rates for  $L_{ig} = 50 \text{ m}$  quickly reach  
 467 a quasi-steady value. The dependence of the spread rate on the wind speed is well predicted by  
 468 WFDS. The quantitative agreement of WFDS is also good, however it is important to note that  
 469 the sensitivity of WFDS to realistic variations in environmental variables (wind speed, moisture  
 470 content, etc.) has not yet been assessed.

471 Another important issue is how the value of the wind speed,  $U_2$ , is obtained. As discussed in  
 472 the previous section, both Eq. 2 and Eq. 3 and WFDS use a value of  $U_2$  that is the average wind

speed at a height of approximately 2 m. In BehavePlus the default height of the wind speed is at the mid-flame height. The experimentally observed average mid-flame height, for  $U_2 = 4.8 \text{ m s}^{-1}$ , was 1.3 m for this fuel and the mid-flame wind speed was  $4.5 \text{ m s}^{-1}$ . With  $U_2 = 4.8 \text{ m s}^{-1}$  input into BehavePlus for the mid-flame wind speed,  $R = 4.4 \text{ m s}^{-1}$  (this plotted in Fig. 7). With the mid-flame wind speed input into BehavePlus,  $R = 3.9 \text{ m s}^{-1}$ . This still significantly over predicts the spread rate of the head fire. The over prediction of the spread rate by Behave for fuels with a surface-to-volume ratio of  $13100 \text{ m}^{-1}$ , which is similar to the fuel used here ( $\sigma = 12240 \text{ m}^{-1}$ ) has been noted before (Gould (1988)).

#### 4.4 Effect of fire head width on fire spread

After  $U_2$ , the head-fire width,  $W$ , was observed to account for the greatest variation in spread rate in the grassland experiments. The correlation between  $R$  and the measured moisture content of dead grass  $M$  was not significant. This was attributed to difficulties with sampling and handling techniques of  $M$ , the relatively small range of  $M$  during the experiments, and to the large effect of wind speed masking the effect of moisture content. Cheney and Gould (1995) found that  $R_o$ , for a given  $U_2$ , rapidly increased as  $W$  increased. For lower wind speeds ( $U_2 < 3.5 \text{ ms}^{-1}$ ),  $R_o$  appeared to asymptote when  $W \cong 50 \text{ m}$ . For  $U_2 > 3.5 \text{ ms}^{-1}$  both  $R_s$  and the value of  $W$  at which  $R_o \approx R_s$  increased. Cheney et al. (1993) comment that models developed from experimental fires that have not been allowed to burn to a substantial size ( $W > 100 \text{ m}$ ) are likely to under predict the spread rates of wildfires, particularly at higher wind speeds.

Figure 7 shows the head fire spread rate versus the head fire width for  $U_2 = 1 \text{ m s}^{-1}$  and the four different lengths of the ignition line fire,  $L_{ig} = 8 \text{ m}, 25 \text{ m}, 50 \text{ m}$  and  $100 \text{ m}$ . The solid line is the spread rate from Eq. (2). The simulations reproduced the trend of an increasing head fire spread rate with an increasing width of the head fire. The head width increased monotonically with time (not shown). All ignition line length cases, with the possible exception of  $L_{ig} = 8 \text{ m}$ , reach a quasi-steady spread rate that is within 25% of the Eq. (3) value. Longer ignition line cases reach spread rates that are closer to the Eq. (3) value (i.e., the plateau value of the solid line). The experimental fires, as described by Eq. (2), obtained a quasi-steady spread rate at narrower head fires than the simulated fires. Figure 8(a-d) are sequential snapshots of the burning region (shaded contours of the mass loss rate are shown) for each of the ignition line fire lengths used. Note that for the  $L_{ig} = 50 \text{ m}$  and  $100 \text{ m}$  cases, Fig. 8(c,d) respectively, the flank fires reach the upper and lower fire breaks.

In Fig. 9 results with  $U_2 = 5 \text{ m s}^{-1}$  are shown. In the left column the location of the leading edge of the head fire (solid line) versus time from WFDS is plotted. Each row in Fig. 9 corresponds to a different ignition line fire length. Also shown in the left column are the width (dashed line) and depth (dotted line) of the head fire. In each case an initial time period of relatively rapid spread is present, followed by a slower spread rate. This initial rapid spread may depend on the ignition procedure, and needs to be investigated. In order to compare to experimental fire behavior, the location of the head fire is also determined using the empirical relation, Eq. (2) (circles). This equation is implemented using  $W$  calculated by WFDS and  $U_2 = 5 \text{ m}^{-1}$ . For the cases with  $L_{ig} = 25 \text{ m}, 50 \text{ m}$ , and  $100 \text{ m}$  WFDS predictions of the head fire location agree well, overall, with those derived from Eq. (2). At the latest time WFDS does over predict the location of the head fire, but by less than 8%. When  $L_{ig} = 8 \text{ m}$  there is an initial period of time, greater than 30 s, during which the head fire spread rate increases before reaching an more quasi-steady value after  $t \cong 110 \text{ s}$ . The head width (dashed line) at which the simulated head fire spreads in a quasi-steady manner is approximately  $W = 65 \text{ m}$  (note Fig. 7 shows similar results for  $U_2 = 1 \text{ m s}^{-1}$ ). This is consistent with experimental observations that spread rates are relatively unaffected by  $L_{ig}$  when  $L_{ig} > 75 \text{ m}$ .

and  $U_2$  is sufficiently small. Relatively little change in the head fire width occurs for  $L_{ig} = 100$  m. Cheney and Gould (1995) note at their highest wind interval between 4.7 and 7.1 m s<sup>-1</sup> a head fire width of more than 125 m in open grassland is required to get spread rates within 10 percent of the quasi-steady rate of spread. Thus, with an ignition line of 100 m, spread rates could still be increasing at wind speeds of 5 m s<sup>-1</sup>. The oscillations in the location of the head fire and fire depth (mostly clearly seen Fig. 9(b)) are due to interactions of the fire plume and the local wind field. Note that increases in  $R$  are associated with increases in  $d$ .

Figure 9 (right column) shows the fire perimeter at 60 s intervals. The relatively high wind speed results in head fire depths (10 m - 12 m) that are greater than the flank fire depths (5 m - 7 m). This does not occur in the weak wind case ( $U_2 = 1$  m s<sup>-1</sup> in Fig. 8). This behavior is consistent with field observations. The average head fire depth from field measurements for  $L_{ig} = 175$  m and  $U_2 = 4.8$  m s<sup>-1</sup> is  $d = 10$  m. Observed fire depths were interpreted from oblique photographs which were rectified and plotted onto a planar map of time isopleths of fire perimeter and fire depth.

#### 4.5 Residence time, mass flux, heat release rate

Figure 10 is a plot of the head fire residence time,  $\tau$ , versus the spread rate of the head fire. Residence times from the WFDS simulations, Australian (AU) experiments, and an empirical formula from Anderson (1969) are plotted on the figure. In the empirical formula the residence time,  $\tau \equiv dR^{-1}$ , is a function only of the surface-to-volume ratio:

$$\tau \equiv \frac{d}{R} = \frac{75600}{\sigma_s}. \quad (4)$$

Sneeuwjagt and Frandsen (1977) tested Eq. (4) and state it provided a good fit to data from their grassland fire experiments. The value of  $\tau$  from Eq. (4), using  $\sigma_s$  for the two AU grassland experiments C064 and F19, is shown in Fig. 10 as horizontal lines labelled C064e and F19e. The value of  $\sigma_s$  is 9770 m<sup>-1</sup> and 12240 m<sup>-1</sup> for C064e and F19e, respectively (see Table 1). The value of  $\tau$  based on measured values of  $d$  and  $R$  in the AU experiments are denoted by C064AU and F19AU. Symbols mark the value of  $\tau$  from WFDS predictions of  $d$  and  $R$  for a range of  $L_{ig}$  and  $U_2$  conditions with F19 grassland fuel. The value of the depth of the head fire,  $d$ , is in the direction of spread (see Fig. 3). C064s or CF19s denote WFDS results for conditions identical to the two AU experiments. WFDS values of  $\tau$  are larger than those from Eq. (4); but only weakly dependent on  $R$  (especially for the larger  $L_{ig}$  values ), which is consistent with Eq. (4).

An important implication of Eq. (4) is that the mass loss rate ( $\dot{m}_s''$ , kg s<sup>-1</sup>m<sup>-2</sup>), and therefore the reaction intensity ( $I_R$ , kW m<sup>-2</sup>), averaged over the time interval  $\tau$  are constant for a given  $\sigma_s$ :

$$I_R = \Delta h_c \frac{1}{\tau} \int_0^\tau \dot{m}_s'' dt = \frac{\Delta h_c (1 - \chi_{char}) w_s}{\tau} = \frac{\Delta h_c (1 - \chi_{char}) w_s \sigma_s}{75600}. \quad (5)$$

The reaction intensity and the commonly used fireline intensity,  $I$  (kW m<sup>-1</sup>), are also related:

$$I = I_R d = I_R R \tau = \Delta h_c (1 - \chi_{char}) w_s R, \quad (6)$$

where  $\Delta h_c (1 - \chi_{char}) w_s$  is the heat per unit area released in the combustion process (neglecting heat from char oxidation). The fireline intensity has a number of practical uses since it has been related to observed flame heights and to fire management guidelines (e.g., Chandler et al. (1983)). By integrating  $I$  along the fire perimeter the total heat release rate, HRR (kW), for that portion of the perimeter can be found. Boundary conditions on large scale atmospheric models require values

548 of HRR.

549 Figure 11 shows the time history of WFDS predictions of  $\dot{m}_s''$  spatially averaged over the fire  
550 beds of the head fire, the flanking fires, and entire fire perimeter. Two different wind cases, each  
551 with  $L_{ig} = 100$  m, are plotted: in Fig. 11(a)  $U_2 = 1 \text{ m s}^{-1}$  and in Fig. 11(b)  $U_2 = 5 \text{ m s}^{-1}$ . In  
552 each case, the average mass flux is largest in the head region of the fire perimeter, due to flame tilt.  
553 However, the flanking fires can be a greater portion of the entire fire line. This is the case for  $U_2$   
554 = 5 m s<sup>-1</sup> as seen in Fig. 9(d). The total mass flux varies within 15% of its mean value for most  
555 of the  $U_2 = 1 \text{ m s}^{-1}$  case (after the fluctuations from ignition have died off) and for the latter half  
556 of the  $U_2 = 5 \text{ m s}^{-1}$  case.

The total HRR of the head fire, the flanking fires, and the entire fire bed for the same two cases  
is displayed in Fig. 12. These HRR values are computed by summing the mass fluxes over each  
region of the actively burning fireline:

$$HRR_{FR} = \int_{FR} Id\ell \cong \sum_{FR} \Delta h_c (1 - \chi_{char}) \dot{m}_s'' \Delta x \Delta y, \quad (7)$$

557 where  $FR$  denotes the head fire or flank fire region of the fire line and  $\Delta x$ ,  $\Delta y$  are the horizontal  
558 dimensions of the grid. After the fire line reaches the edges of the grassland plot at approximately  $t$   
559 = 180 s in the  $U_2 = 1 \text{ m s}^{-1}$  case (see Fig. 8(d)) the flanking fires begin shortening and eventually  
560 disappear, no longer contributing to the HRR in Fig. 12(a). As the flanking fires shorten, the head  
561 fire lengthens and its HRR increases until, at  $t = 350$  s, it spans nearly the entire 200 m grass plot.  
562 In Fig. 12(b) the stronger ambient wind lengthens the flanking fires (see Fig. 9(d)) causing their  
563 HRR (and therefore the total HRR) to increase over the latter part of the simulation.

## 564 4.6 Case studies

565 The mechanism of fire spread can change along the fire perimeter depending on the wind speed.  
566 In zero ambient wind, entrainment by the fire creates a local wind into which the entire fire line  
567 spreads (backing fire). In the presence of an ambient wind, the downwind portion of the fire  
568 perimeter spreads with the wind (heading fire), the upwind portion of the fire perimeter spreads  
569 into the wind (backing fire), and the sides or flanks of the fire perimeter spread under conditions  
570 that can alternate between heading and backing fires. Note that in the cases considered here,  
571 there are no backing fires since ignition occurred along the fire break at the upwind border of the  
572 plot. Backing fires, in which the flame tends to tilt away from the unburned fuel, can consume  
573 the fuel from the base upward, resulting in more complete fuel consumption. Heading fires, in  
574 which the flame tilts toward the unburned fuel, can be associated with lower fuel consumption  
575 because the grass ignites at the top and burns downward, covering the unburned fuel beneath  
576 with a protective coating of ash. The spread mechanism in a flank fire can involve, depending on  
577 the fire/wind interaction, both the burning downward mechanism of head fires and the burning  
578 upward mechanism of backing fires. Thus, modeling the evolution of the entire fire line is a greater  
579 challenge, due to the different spread mechanisms, than modeling the behavior of just the head fire.

580 WFDS can not directly resolve the details in the grass fuel bed that differentiate a backing fire  
581 from a heading fire since the entire fuel bed is unresolved on the gas phase computational grid. For  
582 example, the height of the first grid cell in WFDS simulations of experiment F19 is 1.4 m while  
583 the height of the grass is 0.51 m. However, the fire/atmosphere interactions that occur over larger  
584 scales are much better resolved. It is hoped that this level of resolution of the fire physics will  
585 be sufficient to capture the dynamics of the entire fire perimeter. It is important that a three-  
586 dimensional model predict the behavior of the entire fire perimeter. Otherwise, the overall heat

587 release rate, fuel consumption, and smoke generation will be (to some degree) incorrectly predicted.  
588 The potential for this was seen, for example, in Fig. 12(b) where the gradual lengthening of the flank  
589 fire increased the total HRR of the fire while the HRR contribution from the head fire remained  
590 constant. These global fire characteristics are particularly important inputs to landscape and  
591 regional smoke transport models, which do not attempt to model the fire/fuel physics. In addition,  
592 the mechanisms behind extreme fire behavior (such as blow ups) are still poorly understood. A  
593 model that simulates the behavior of the entire fire perimeter, as opposed to only the head fire, is  
594 more likely to shed light on these issues.

595 In this section, model predictions of fire perimeters from two experimental cases are presented.  
596 In the first experiment, called F19, the fuel is *Themeda* grass ( $\sigma_s = 12240 \text{ m}^{-1}$ ). The grassland  
597 plot is 200 m x 200 m and the ignition line fire is 175 m long. This line fire was created with  
598 drip torches carried by two field workers walking for 56 s (87.5 m) in opposite directions from the  
599 center point to the ends of the line fire. The average wind speed, measured at the corners of the  
600 grassland plot and not including measurements influenced by the fire, equaled  $4.8 \text{ m s}^{-1}$ . In the  
601 second experiment considered, called C064, the fuel is *Eriachne* grass ( $\sigma_s = 9770$ ). This grass was  
602 cut to 50 % of its height with the cuttings removed. The grassland plot is 104 m x 108 m and the  
603 ignition line was 50 m long. The ignition line fire was created with drip torches carried by field  
604 workers walking in opposite directions for 26 s (25 m). The average wind speed was  $4.6 \text{ m s}^{-1}$ .  
605 Fuel bed characteristics are given in Table 1 for both experiments. WFDS simulates the ignition  
606 procedure by sequentially igniting strips of the fuel bed at a rate that matches the experimental  
607 procedure.

608 The time history of  $U_2$  from WFDS and experiment F19 and C064 are shown in Fig. 13(a) and  
609 Fig. 14(a), respectively. The experimental value of  $U_2$  (filled circles) is the average of the magnitude  
610 of the velocity vector, averaged over 5 s, in the horizontal plane  $z = 2 \text{ m}$  measured every five seconds  
611 at the two upwind corners of the grassland plot. The WFDS value of  $U_2$  is the magnitude of the  
612 simulated velocity vector at the  $y$  midpoint of the ignition line fire and at a height of  $z = 2.1 \text{ m}$   
613 and  $z = 1.95 \text{ m}$  for cases F19 and C064, respectively.

614 WFDS velocity vector components in the horizontal plane  $z \cong 2 \text{ m}$  are shown in Fig. 13(b) and  
615 Fig. 14(b) for cases F19 and C064, respectively. Also shown is the outer boundary of the flaming  
616 region in the same plane,  $z \cong 2 \text{ m}$ . Case F19 clearly has a larger fire perimeter. F19 also presents  
617 a greater blockage to the ambient wind as can be seen by the smaller vector lengths in Fig. 13(b),  
618 compared to Fig. 14(b), upwind of the head fire. Entrainment of air toward the fire from the  
619 far-field can be clearly seen.

620 Figures 15(a,b) contain the location of the leading edge of the head fire versus time, from both  
621 WFDS (solid line) and by using Eq. (2) (circles) for both experimental cases F19 and C064, re-  
622 spectively. The head width from WFDS is plotted as a dashed line. The head depth from both  
623 WFDS (dotted line) and its average value from the experiments (dash-dot line) are also shown.  
624 The average value of the WFDS head fire depths is 11.4 m for case F19 (experimental value was  
625 10 m) and 12.2 m for case C064 (experimental value was 7.1 m). Overall, the spread rate of both  
626 cases agrees well with the empirical formula, Eq. (2). During the period of transient behavior in  
627 case F19,  $76 \text{ s} \leq t \leq 90 \text{ s}$  in 15(a), the simulated flanking fires reach the boundaries of the grassland  
628 plot and extinguish. Before and after this period the simulated flame spread rate is nearly constant  
629 and in good agreement with Eq. (2).

630 The fire perimeters of cases F19 and C064 are shown in Figs. 16(a,b), respectively. The actively  
631 burning fire bed from WFDS is shown as shaded contours. The leading edge of the head fire from  
632 the simulations is plotted as symbols. In F19 a wind shift occurs in the experiment after  $t = 86 \text{ s}$   
633 which breaks the symmetry of the fire perimeter. This does not occur in WFDS since a constant  
634 wind orientation is assumed at the inflow boundary. As expected from the previous results, the

635 spread of the head fire is well predicted at all times. The simulated fire reaches the downwind fire  
636 break at 133 s; the experimental fire at 138 s. Before the wind shift, the predicted fire perimeter  
637 closely matches the measured fire perimeter. After  $t = 86$  s it is not clear how well WFDS performs  
638 because the wind shift significantly changes the observed fire perimeter. Also, long flanking fires  
639 (as, for example, those shown in Fig. 9(c)) do not develop for this case because the flank fires reach  
640 the fire breaks relatively soon.

641 In case C064, shown in Fig. 16(b) extended free burning flank fires do develop. The spread rate  
642 of the head fire is well predicted. WFDS over predicts the spread rate of the flank fires. The reasons  
643 for this are the subject of ongoing model development efforts. The current version of WFDS does  
644 not faithfully model the upward spread mechanism that can be present in flank fires. Instead, the  
645 fire burns downward through the grassland fuel bed everywhere along the perimeter. Also, flank fire  
646 depths in the field were observed to be significantly smaller than head fire depths. The horizontal  
647 grid resolutions used here (1.66 m) adequately resolve the head fire depth but this may not be the  
648 case for the flank fires.

649 Figures 17(a,b) are plots of the spatially averaged mass flux in the head and flank fire regions of  
650 the fire perimeter and the total perimeter for case F19 and C064, respectively. Case C064 has a  
651 smaller mass flux which is consistent with its smaller fuel load. The initial period of larger mass  
652 flux in F19 ( $t < 60$  s) is due to the ignition line fire. The ignition procedure stops at  $t = 56$  s.  
653 Figures 18(a,b) show the heat release rates associated with the entire fire perimeter and the head  
654 and flanking fires for both experimental cases. The HRR in case C064 is significantly smaller than  
655 F19 due to its lighter fuel loading and shorter fireline perimeter. In case F19, the flanking fires  
656 dominate the total HRR during the ignition phase. During the latter part of the F19 case  $HRR \cong 1.4$  GW  
657 (or  $I_R = 350$  kW m $^{-2}$ ). For comparison, estimates of  $I_R$  during the burning of logging  
658 slash are approximately  $I_R = 75$  kW m $^{-2}$  (Ohlemiller and Corley 1994). The actively burning area  
659 in the logging slash fire was approximately  $2 \times 10^5$  m $^2$ . This is 50 times larger than the actively  
660 burning area in the latter half of the F19 simulation. For this reason the total HRR in the logging  
661 slash fires was 15 GW, approximately 10 times larger than the F19 grassland fire.

662 The spatially averaged head fire mass flux in Figs. 17(a,b) is used in Eq. (5) to determine the  
663 time history of  $I_R$  for the head fire (not shown). The time history of  $I$  for the head fire is then  
664 determined from  $I_R$  and  $d$  by using Equation (6). The resulting head-fireline intensity is plotted  
665 (solid line) in Figs. 19(a,b) for case F19 and C064, respectively. Also plotted are the values of  $I$   
666 determined from the experimentally observed head fire spread rates using the last relation on the  
667 right-hand-side of Eq. (6) (line labelled ‘R based’) and from the semi-empirical model BehavePlus  
668 (line labelled ‘BEHAVE’). The experimentally observed head fire spread rates are  $R = 1.4$  m s $^{-1}$ ,  
669 1.2 m s $^{-1}$  for F19 and C064, respectively. For these experimental conditions the simple approach  
670 using the head fire spread rate provided a better estimate of  $I$  than BehavePlus. The BehavePlus  
671 values were obtained by using the experimentally measured values of fuel load, moisture, surface-  
672 to-volume ratio, and fuel bed depth which are listed in Table 1, and the average of measured values  
673 for the moisture of extinction (22 %, Cheney et al. (1998)). The mid-flame wind speeds of 4.4  
674 m s $^{-1}$  for F19 and 2.8 m s $^{-1}$  for C064 were used. The dead fuel heat content was 18608 kJ  
675 kg $^{-1}$ , which is listed in NFFL descriptions for grass fuels UCSB (2005). BehavePlus predictions  
676 of the head-fireline intensity are nearly a factor of two too large for case F19 and a factor of four  
677 too small for case C064. This is due to BehavePlus over predicting the spread rate for F19 ( $R$   
678 = 4.4 m s $^{-1}$ ) and under predicting it for C064 ( $R = 0.47$  m s $^{-1}$ ). This is relevant to mesoscale  
679 coupled atmosphere-fire models currently under development (e.g., Clark et al. (2003, 2004) and  
680 Coen (2005)) since their heat and mass fluxes from the fire into the atmosphere are based in part  
681 on spread rate predictions from empirical and semi-empirical spread rate formulas. These results  
682 imply that, for AU grassland fuels, the empirical fire spread formula should be used rather than

683 the semi-empirical (Rothermel 1972) spread rate.

## 684 5 Summary and Conclusions

685 A physics-based, transient, three-dimensional, coupled fire-atmosphere model for simulating fire  
686 spread through surface fuels on flat terrain, was developed and evaluated using observational data  
687 from Australian grassland fires. This model, called WFDS, is an extension, to vegetative fuels, of  
688 the structural Fire Dynamics Simulator (FDS) developed at the National Institute of Standards  
689 and Technology (NIST). Grassland fires were chosen here because of the simplicity of both the fuel  
690 and terrain, and because a significant amount of experimental data (for Australian grassland fires)  
691 exists for model validation.

692 Sixteen fires (four different ignition line lengths and four different wind speeds) were simulated.  
693 Head fire spread rates from WFDS were compared to an empirical relation developed from exper-  
694 imental data. Overall, WFDS predictions of the dependence of the head fire spread rate on both  
695 the ambient wind speed and on the head fire width were similar to an empirical relation.

696 Two specific Australian grassland experiments were also simulated. In both cases the location  
697 of the head fire was well predicted. One experimental case had extended, freely spreading, flank  
698 fires. WFDS over predicted the spread rate of these flank fires. The reasons for this are under  
699 investigation. One possibility is that flank fires are under resolved, since their fire depth can be  
700 significantly smaller than head fires. Some light may be shed on this issue by comparing to a larger  
701 number of experimental fires. We plan to extend the validation effort to a larger set of experiments  
702 and to a wider range of fuel parameters (moisture, surface to volume ratio, packing ratio) in order  
703 to better assess WFDS capabilities.

704 Areas for further model development and model evaluation include:

- 705 • The vegetation model is not appropriate for fuels through which significant vertical flame  
706 spread can occur. A model approach for suspended vegetation, such as tree crowns, has been  
707 implemented and is currently being evaluated. Preliminary results can found in Mell et al.  
708 (2005a).
- 709 • The grassland fuel bed is assumed to burn from the top down. This is consistent with field  
710 observations of head fires, which spread with the ambient wind. It is not consistent with  
711 backing or flanking fire behavior, based on observations. This may play a role in the over  
712 prediction of flank fire spread rates.
- 713 • Char oxidation has not been considered. For this reason, smoldering or glowing combustion of  
714 the fuel after the fire front has passed is not present. This can be an important contribution  
715 to overall smoke generation.
- 716 • The underestimation of convective heat transfer into the solid fuel in regions of active com-  
717 bustion, and the sensitivity of the results to changes in how the drag and convective heat  
718 transfer is modeled needs further investigation.
- 719 • A more complete evaluation of the model's performance for a range of fuel and environmental  
720 parameters (e.g., moisture level, surface-to-volume ratios, bulk fuel loadings, wind speeds,  
721 and wind profiles) is required.

722 Multidimensional numerical fluid-dynamical wildfire simulation models can be used to study  
723 the behavior of wildfire and wildland-urban interface fires. However, depending on the scope of  
724 the physical models employed they can require computational resources that preclude real-time

725 forecasts. Such is the case with the version of WFDS presented here. This model, therefore, has  
726 not been designed to replace operational models, but it can be used to expand or improve their  
727 capabilities.

728 The computational cost of physics-based wildland fire modeling limits the application of the  
729 approach to modeling wildfire behavior within a certain scale range. In models like WFDS, com-  
730 putational resources are devoted to resolving fire combustion and the close-in fire-atmosphere  
731 flow. In large-scale coupled atmosphere-wildfire models the thermal degradation of solid fuel is  
732 not modeled directly and combustion is parameterized. Empirical or semi-empirical models for  
733 fire spread rates and heat and mass fluxes from the fire to the atmosphere are used (Clark et al.  
734 1996, 2003, 2004; Coen 2005). Computational resources can then be devoted to resolving the large  
735 scale fire-atmospheric physics.

736 Large scale fire-atmosphere interactions are considered to be of major importance to predicting  
737 fire behavior, especially severe fire behavior. A longer term goal, therefore, is to develop and test  
738 (using WFDS) improved models of fire physics suitable for use in large scale atmosphere-wildfire  
739 models. Once suitably validated, both the WFDS and a large scale coupled atmosphere-wildfire  
740 model can be used to evaluate operational models over a wide range of conditions and real-time  
741 applications, such as prediction of firebrand generation and transport, and fire spread rates. They  
742 can also be used to improve our understanding of how fuel conditions (amount, type, moisture  
743 content), terrain and weather are responsible for severe and blow-up fires.

744 Another long term goal at NIST is the development of a simulation tool for wildland-urban inter-  
745 face fires. The cost in insured damages from these fires can significantly outweigh the operational  
746 costs of fighting the fire. The fuels in these fires are an intermix of continuous and discrete vege-  
747 tative fuels and structural materials. These fuel types, and their spatial arrangement, fall outside  
748 traditional wildland fuel classification methods and, therefore, current fire-risk assessment methods  
749 or models. A suitably validated simulation tool could be used to help determine and assess the  
750 important risk factors in existing and planned communities.

## 751 6 Acknowledgements

752 The first author would like to thank Dr. Ron Rehm of NIST for many fruitful discussions during  
753 the writing of this paper. This work was sponsored in part by the USDA Forest Service Joint  
754 Venture Agreement 03-JV-11231300-088.

## 755 References

- 756 F.A. Albini. Estimating wildfire behavior and effects. Technical Report USDA For. Serv. Gen.  
757 Tech. Rep. INT-30, USDA Forest Service, 1976.
- 758 F.A. Albini. A model for fire spread in wildland fuels by radiation. *Combust. Sci. and Tech.*, 42:  
759 229–258, 1985.
- 760 F.A. Albini. Wildland fire spread by radiation – a model including fuel cooling by natural convec-  
761 tion. *Combust. Sci. and Tech.*, 45:101–113, 1986.
- 762 F.A. Albini. *Fire in the Environment: The Ecological, Atmospheric, and Climatic Importance of*  
763 *Vegetation Fires*, chapter 3. Dynamics and modeling of vegetation fires: Observations. John  
764 Wiley and Sons, 1993.

- 765 H.E. Anderson. Heat transfer and fire spread. Technical Report USDA For. Serv. Res. Pap. INT-69,  
766 USDA Forest Service, 1969.
- 767 P.L. Andrews. BEHAVE: Fire behavior prediction and modeling system – BURN subsystem part  
768 1. Technical Report USDA For. Serv. Gen. Tech. Rep. INT-194, USDA Forest Service, 1986. 130  
769 pp. program available at <http://fire.org>.
- 770 P.L. Andrews, C. D. Bevins, and R. C. Seli. BehavePlus fire modeling system, version 2.0: User's  
771 Guide. Technical Report USDA For. Serv. Gen. Tech. Rep. RMRS-GTR-106WWW, USDA  
772 Forest Service, 2003. 132 pp. program available at <http://fire.org>.
- 773 M. Appicello. Federal wildland policy. [www.fs.fed.us/land/wdfire.htm](http://www.fs.fed.us/land/wdfire.htm) (as of 7/12/04), 1996.
- 774 A. Atreya. *Pyrolysis, ignition and fire spread on horizontal surfaces of wood*. PhD thesis, Harvard  
775 University, 1983.
- 776 C.P. Bankston, B.T. Zinn, R.F. Browner, and E.A. Powell. Aspects of the mechanisms of smoke  
777 generation by burning materials. *Combustion and Flame*, 41:273–292, 1981.
- 778 H.R. Baum and W.E. Mell. A radiative transport model for large-eddy fire simulations. *Combust.  
779 Theory Modelling*, 2:405–422, 1998.
- 780 T. Beer. The interaction of wind and fire. *Boundary-Layer Meteorology*, 54:287–308, 1991.
- 781 J.B. Bell, N.J. Brown, M.S. Day, M. Frenklach, J.F. Grcar, and S.R Tonse. The Dependence of  
782 Chemistry on the Inlet Equivalence Ratio in Vortex-Flame Interactions. *Proc. Combustion Inst.*,  
783 28:1933–1939, 2000.
- 784 R.W. Bilger. *Turbulent Reacting Flows*, chapter 4. Turbulent Flows with Nonpremixed Reactants.  
785 Springer–Verlag, 1980.
- 786 USFS BlueSky. Bluesky modeling framework to predict cumulative impacts of smoke from agricul-  
787 tural, forest, and range fires, 2004. <http://www.fs.fed.us/bluesky/>.
- 788 B.W. Butler. . In *Proceedings: 12th Conference of Fire and Forest Meteorology*, 1993. p. 26.
- 789 C. Chandler, P. Cheney, L. Thomas, P. Trabaud, and D. Williams. *Fire in Forestry*. John Wiley  
790 & Sons, 1983. Chap. 1.
- 791 N.P. Cheney and J.S. Gould. Fire growth in grassland fuels. *Int. J. of Wildland Fire*, 5(4):237–247,  
792 1995.
- 793 N.P. Cheney, J.S. Gould, and W.R. Catchpole. The influence of fuel, weather and fire shape  
794 variables on fire spread in grasslands. *Int. J. of Wildland Fire*, 3(1):31–44, 1993.
- 795 N.P. Cheney, J.S. Gould, and W.R. Catchpole. Prediction of fire spread in grasslands. *Int. J. of  
796 Wildland Fire*, 9(1):1–13, 1998.
- 797 T.L. Clark, J.L. Coen, and D. Latham. Description of a coupled atmosphere-fire model. *Intl. J.  
798 Wildland Fire*, 13(1):49–63, 2004.
- 799 T.L. Clark, M. Griffiths, M.J. Reeder, and D. Latham. Numerical simulations of grassland fire in  
800 the Northern Territory, Australia: A new subgrid-scale fire parameterization. *J. of Geophysical  
801 Res.*, 108(D18):doi: 10.1029/2002JD003340. issn: 0148–0227, 2003.

- 802 T.L. Clark, M.A. Jenkins, J. Coen, and D. Packham. A coupled atmospheric-fire model: Convective  
803 feedback on fire-line dynamics. *J. Applied Meteorology*, 35:875–901, 1996.
- 804 J. Coen. Simulation of the Big Elk Fire using coupled atmosphere-fire modeling. *Infl. J. Wildland  
805 Fire*, 14:49–59, 2005.
- 806 J.L. Coen. Simulation of wildfire incidents using coupled atmosphere-fire modeling. In *Second  
807 International Wildland Fire Ecology and Fire Management Congress and Fifth Symposium of  
808 Fire on Forest Meteorology*. American Meteorological Society, 2003. paper J2.4.
- 809 J.J. Colman and R.R. Linn. Non-local chemistry implementation in HIGRAD/FIRETEC. 2003.
- 810 J.J. Colman and R.R. Linn. Separating combustion from pyrolysis in HIGRAD/FIRETEC. 2005.
- 811 A.M. Costa, J.C.F. Pereira, and M. Siqueira. Numerical prediction of fire spread over vegetation  
812 in arbitrary 3D terrain. *Fire and Materials*, 19:265–273, 1995.
- 813 K.P. Davis. *Forest Fire: Control and Use*. McGraw-Hill, New York, 1959.
- 814 N.J. De Mestre, E.A. Catchpole, D.H. Anderson, and R.C. Rothermel. Uniform propagation of a  
815 planar fire front without wind. *Combust. Sci. and Tech.*, 65:231–244, 1989.
- 816 C. Di Blasi. Modeling and simulation of combustion processes of charring and non-charring solid  
817 fuels. *Prog. Energy Combust. Sci.*, 19:71–104, 1993.
- 818 A.P. Dimitrakopoulos. . *J. Anal. Appl. Pyrol.*, 60:123, 2001.
- 819 J.L. Dupuy and D. Morvan. Numerical study of the a crown fire spreading toward a fuel break  
820 using a multiphase physical model. *International Journal of Wildland Fire*, 14:141–151, 2005.
- 821 M.A. Finney. FARSITE: Fire Area Simualtor-Model, Development and Evaluation. Technical  
822 Report RMRS-RP-4, USDA Forest Service, Rocky Mountain Research Station Paper, 1998.
- 823 W.L. Fons. Analysis of fire spread in light forest fuels. *J. Agricultural Research*, 72(3):93–121, 1946.
- 824 G.P. Forney and K.B. McGrattan. User's Guide for Smokeview Version 4: A Tool for Vi-  
825 sualizing Fire Dynamics Simulation Data. Technical Report NISTIR Special Publication,  
826 1017, National Institute of Standards and Technology, Gaithersburg, Maryland, August 2004.  
827 <http://fire.nist.gov/bfrlpubs/>.
- 828 GAO. Western national forests: A cohesive strategy is need to address catastrophic wildfire threats.  
829 Technical Report GAO/RCED-99-65, Committee on Resources, House of Representatives, April  
830 1999. Report to the Subcommittee on Forests and Forest Health.
- 831 GAO. Technology Assessment: Protecting Structures and Improving Communications during Wild-  
832 land Fires. Technical Report GAO-05-380, United State Government Accountability Office, April  
833 2005. Report to Congressional Requestors.
- 834 J.S. Gould. Validation of the Rothermel fire spread model and related fuel parameters in grasslands  
835 fuels. CSIRO, Canberra, July 11-12 1988.
- 836 A.M Grishin. *Fire in Ecosystems of Boreal Eurasia*, chapter Mathematical modelling of forest fires.  
837 Kluwer Academic Publishers, 1996.

- 838 A.M. Grishin, A.D. Gruzin, and V.D. Zverev. Study of the structure and limits of propagation of  
839 the front of an upstream forest fire. *Fizika Gorenija i Vzryva*, 21(9), 1985.
- 840 K.G. Hirsch. Canadian forest fire behavior prediction (FBP) system: user's guide. Technical Report  
841 Special Report 7, Canadian Forest Service, Northwest Region, Northern Forestry Centre, 1996.  
842 122 pp.
- 843 J.P. Holman. *Heat Transfer*. McGraw-Hill, New York, 5th edition, 1981. page 285.
- 844 W.Q. Hough. Caloric value of some forest fuels of the southern United States. Technical Report  
845 USDA Foerst Service Research Note SE-120, Southeastern Forest Experiment Station, South-  
846 eastern Forest Experiment Station, Ashville, North Carolina, US Dept. of Agriculture, Forest  
847 Service, 1969. 6 pp.; <http://www.srs.fs.usda.gov/pubs>.
- 848 F.P. Incropera and D.P. Dewitt. *Fundamentals of Heat and Mass Transfer*. John Wiley & Sons,  
849 4th edition, 1996. page 846.
- 850 P.G. Jarvis, G.B. James, and J.J. Lansberg. *Vegetation and the Atmosphere, Vol. 2 case studies*,  
851 chapter 7. Coniferous Forest, pages 172–240. Academic Press, New York, 1976.
- 852 E.A. Johnson and K. Miyanishi, editors. *Forest Fires: Behavior and Ecological Effects*. Academic  
853 Press, 2001.
- 854 H. Koseki and G.W. Mulhooand. The effect of diameter of the burning of crude oil pool fires. *Fire  
Technology*, 54, 1991.
- 855 M. Larini, F. Giroud, B. Porterie, and J.-C. Loraud. A multiphase formulation for fire propagation  
856 in heterogeneous combustible media. *Int. J. Heat Mass Transfer*, 41:881–897, 1998.
- 857 R. Linn and P. Cunningham. Numerical simulations of grass fires using a coupled atmosphere-fire  
858 model: Basic fire behavior and dependence on wind speed. *J. Geophysical Res.*, 110, 2005.
- 859 R. Linn, J. Reisner, J.J. Colman, and J. Winterkamp. Studying wildfire behavior using FIRETEC.  
860 *Intnl. J. of Wildland Fire*, 11:233–246, 2002.
- 861 R.R. Linn. *A transport model for prediction of wildfire behavior*. PhD thesis, New Mexico State  
862 University, 1997. also published as Los Alamos Report, LA-13334-T, 1997.
- 863 R.R. Linn. personal communication, 2005.
- 864 J. Margeri and O Sero-Guillaume. Modelling forest fires: Part II: reduction to two-dimensional  
865 models and simulation of propagation. *Intl. J. Heat and Mass Transfer*, 45:1723–1737, 2002.
- 866 K.B. McGrattan. Fire Dynamics Simulator (Version 4), Technical Reference Guide. Editor, Mc-  
867 Grattan, K.B. NISTIR Special Publication, 1018, National Institute of Standards and Technol-  
868 ogy, Gaithersburg, Maryland, June 2004. <http://fire.nist.gov/bfrlpubs/>.
- 869 W. Mell, A. Maranghides, R. Rehm, S. Manzello, G. Forney, M.A. Jenkins, R. Sun,  
870 and S. Krueger. url for preliminary wildland fire modeling results webpage, 2005a.  
871 <http://www2.bfrl.nist.gov/userpages/wmell/public.html>.
- 872 W.E. Mell, J.J. Charney, M.A. Jenkins, P. Cheney, and J. Gould. Numerical simulations of grassland  
873 fire behavior from the LANL-FIRETEC and NIST-WFDS models. EastFIRE Conference, May  
874 11–13 2005b. George Mason University, Fairfax, VA.

- 876 W.E. Mell and J.R. Lawson. A Heat Transfer Model for Firefighters' Protective Clothing. *Fire*  
877 *Technology*, 36:39–68, 2000.
- 878 W.E. Mell, K.G. McGrattan, and H.R. Baum. Numerical simulation of combustion in fire plumes.  
879 *Proc. Combustion Inst.*, 26:1523–1530, 1996.
- 880 W.E. Mell, S.L. Olson, and T. Kashiwagi. Flame spread along free edges of thermally thin samples  
881 in microgravity. *Proc. Combust. Inst.*, 28:473–479, 2000.
- 882 C. Moro. Technical Report. Technical report, INRA Equipe de Pré des Incendies de Forêt, 1997.
- 883 D. Morvan and J.L. Dupuy. Modeling Fire Spread Through a Forest Fuel Bed Using a Multiphase  
884 Formulation. *Comb. Flame*, 127:1981–1984, 2001.
- 885 D. Morvan and J.L. Dupuy. Modeling the propagation of a wildfire through a Mediterranean shrub  
886 using a multiphase formulation. *Comb. Flame*, 138:199–210, 2004.
- 887 D. Morvan, V. Tauleigne, and J.L. Dupuy. Flame Geometry and Surface to Crown Fire Transition  
888 During the Propagation of a Line Fire Through a Mediterranean Shrub. Millpress, Rotterdam,  
889 ISBN 90-77017-72-0, 2002a. also Communications from Fire Star consortiums members at the  
890 IV International Conference on Forest Fire Research, Luso, November 18-21, 2002.
- 891 D. Morvan, V. Tauleigne, and J.L. Dupuy. Wind Effects on Wildfire Propagation Through a  
892 Mediterranean Shrub. Millpress, Rotterdam, ISBN 90-77017-72-0, 2002b. also Communications  
893 from Fire Star consortiums members at the IV International Conference on Forest Fire Research,  
894 Luso, November 18-21, 2002.
- 895 P.J. Murphy, J.P. Mudds, B.J. Stocks, E.S. Kasischke, D. Barry, M.E. Alexander, and N.H.F French.  
896 *Ecological Studies, Vol. 138, Fire, climate change, and carbon cycling in the boreal forest*, chapter  
897 Historical fire records in the North American boreal forest, pages 274–288. Springer-Verlag, New  
898 York, New York, USA, 2000.
- 899 NAS. *A Study of Fire Problems*, chapter Appendix IV: Note on radiative transport problems arising  
900 in fire spread. National Academy of Sciences – National Research Council, Washington, D.C.,  
901 1961. Publication 949.
- 902 I.R. Nobel, G.A.V. Bary, and A.M. Gill. McArthur's fire-danger meters expressed as equations.  
903 *Australian J. of Ecology*, 5:201–203, 1980.
- 904 T. Ohlemiller and D. Corley. Heat release rate and induced wind field in a large scale fire. *Combust.*  
905 *Sci. Tech.*, 97:315–330, 1994.
- 906 M.N. Ozisk. *Radiative Heat Transfer and Interactions with Conduction and Convection*. John  
907 Wiley & Sons, 1st edition, 1973.
- 908 P.J. Pagni and T.G. Peterson. Fire spread through porous fuels. *Proc. Combust. Inst.*, 14:1099–  
909 1107, 1973.
- 910 W.J. Parker. Prediction of the heat release rate of douglas fir. pages 337–346. International  
911 Association for Fire Safety Science, 1989.
- 912 E. Pastor, L. Zarate, E. Planas, and J Arnaldos. Mathematical models and calculations systems  
913 for the study of wildland fire behavior. *Prog. Energy. Combust. Sci.*, 29:139–153, 2003.

- 914 W.M. Pitts. Wind effects on fires. *Prog. Energy. Combust. Sci.*, 17:83–134, 1991.
- 915 B Porterie, D. Morvan, M. Larini, and J.C. Loraud. Wildfire propagation: a two-dimensional  
916 multiphase approach. *Combust. Explos. Shock Waves*, 34:139, 1998. also in Fizika Gorenija i  
917 Vzryva, Vol. 34, p.26, (1998).
- 918 B Porterie, D. Morvan, J.C. Loraud, and M. Larini. Firespread through fuel beds: Modeling of  
919 wind-aided fires and induced hydrodynamics. *Phys. Fluids*, 12(7):1762–1782, 2000.
- 920 J.G. Quintiere. *Principles of Fire Behavior*. Delmar Publishers, 1997.
- 921 G.D. Raithby and E.H. Chui. A Finite-Volume Method for Predicting Radiant Heat Transfer in  
922 Enclosures with Participating Media. *J. Heat Transfer*, 112(2):415–423, 1990.
- 923 R.G. Rehm and H.R. Baum. The Equations of Motion for Thermally Driven, Buoyant Flows.  
924 *Journal of Research of the NBS*, 83:297–308, 1978.
- 925 J. Reisner, S. Wynne, L. Margolin, and R. Linn. Coupled Atmosphere-Fire Modeling Employing  
926 the Method of Averages. *Monthly Weather Review*, 128:3683–3691, 2000.
- 927 S.J. Ritchie, K.D. Steckler, A. Hamins, T.G. Cleary, J.C. Yang, and T. Kashiwagi. The effect of  
928 sample size on the heat release rate of charring materials. pages 177–188. International Associa-  
929 tion for Fire Safety Science, March 3–7 1997.
- 930 D.E. Rosner. *Transport Processes in Chemically Reacting Flow Systems*. Dover Publications, Inc.,  
931 Mineola, New York, 2000.
- 932 R.C. Rothermel. A mathematical model for predicting fire spread in wildland fuels. Technical  
933 report, 1972.
- 934 O. Sero-Guillaume and J. Margeri. Modelling forest fires: Part I: a complete set of equations derived  
935 by extended irreversible thermodynamics. *Intl. J. Heat and Mass Transfer*, 45:1705–1722, 2002.
- 936 J. Smagorinsky. General Circulation Experiments with the Primitive Equations I. The Basic Ex-  
937 periment. *Monthly Weather Review*, 91:99–164, 1963.
- 938 R.J. Sneeuwjagt and W.H. Frandsen. Behavior of experimental grass fires vs. predictions based on  
939 Rothermel's fire model. *Can. J. For. Res.*, 7:357–367, 1977.
- 940 G.L. Stephens. The parameterization of radiation for numerical weather prediction and climate  
941 models. *Monthly Weather Review*, 112:827–867, 1984.
- 942 S. Stewart, V. Radeloff, and Hammer R. Characteristics and location of the wildland-urban interface  
943 in the United States. Novemeber 2003.
- 944 B.J. Stock and A.J. Simard. Forest Fire Management in Canada. *Disaster Managment*, 5(1), 1993.
- 945 R.A. Susott. Characterization of the thermal properties of forest fuels by combustible gas analysis.  
946 *Forest Sci.*, 2:404–420, 1982.
- 947 UCSB. University of southern california, santa barbara: Southern california wildfire hazard center,  
948 2005. <http://www.icesc.ucsb.edu/resac/>.
- 949 R.O. Weber. Modelling fire spread through fuel beds. *Prog. Energy Combust. Sci.*, 17:67–82, 1991.

- 950 F.A. Williams. Urban and wildfire fire phenomenology. *Prog. Energy Combust. Sci.*, 8:317–354,  
951 1982.
- 952 R. Yuen, R. Casey, G. De Vahl Davis, E. Leonardi, G.H. Yeoh, V. Chandrasekaran, and S.J.  
953 Grubits. A three-dimensional mathematical model for the pyrolysis of wet wood. pages 189–200.  
954 Intnl. Assoc. for Fire Safety Science, March 3–7 1997.
- 955 X.Y. Zhou and J.C.F. Pereira. A multidimensional model for simulating vegetation fire spread  
956 using a porous media sub-model. *Fire and Materials*, 24:37–43, 2000.
- 957 J. Zicherman. Fire at the urban wildland interface: Performance of California homes and buildings.  
958 Technical Report IFB No: 5CA334189 FCA No.: 05-6369, Fire Cause Analysis, Richmond, CA,  
959 2004. prepared for California Dept. Forestry and Fire Protection, Rodney Slaughter.

## 960 A Model equations

### 961 A.1 Approach for modeling the gas phase

The governing equations for low Mach number flow with combustion are based on those derived in Rehm and Baum (1978), where it is assumed that pressure changes due to the fire or buoyancy induced flow are a small fraction of the ambient pressure (i.e., the pressure in the absence of the fire). The resulting equations are commonly known as a low Mach number approximation. Explicit second order Runge-Kutta time stepping and second order spatial differencing on a rectilinear grid is used. Additional details, especially of the numerical approach and boundary condition implementation can be found in McGrattan (2004). Ideal gases and Fickian diffusion are assumed. The equation for conservation of total mass is

$$\frac{\partial \rho}{\partial t} + \mathbf{u} \cdot \nabla \rho = -\rho \nabla \cdot \mathbf{u}. \quad (8)$$

962 This equation requires the divergence of the velocity  $\nabla \cdot \mathbf{u}$ . The determination of  $\nabla \cdot \mathbf{u}$  is discussed  
963 in Sec. A.1.1.

964 The equation for conservation of momentum is

$$\frac{\partial \mathbf{u}}{\partial t} + \nabla \mathcal{H} - \mathbf{u} \times \boldsymbol{\omega} = \frac{1}{\rho} [(\rho - \rho_\infty) \mathbf{g} + \nabla \cdot \boldsymbol{\tau} - \mathbf{F}_D], \quad (9)$$

$$\nabla \mathcal{H} = \frac{1}{2} \nabla |\mathbf{u}|^2 + \frac{1}{\rho} \nabla p_d \cong \frac{1}{2} \nabla |\mathbf{u}|^2 + \frac{1}{\rho_\infty} \nabla p_d, \quad (10)$$

$$\boldsymbol{\tau} = \mu_{LES} \left( \text{def } \mathbf{u} - \frac{2}{3} (\nabla \cdot \mathbf{u}) \mathbf{I} \right). \quad (11)$$

965 Here the vector identity  $(\mathbf{u} \cdot \nabla) \mathbf{u} = (1/2) \nabla |\mathbf{u}|^2 - \mathbf{u} \times \boldsymbol{\omega}$  is used and the deformation, or rate of strain,  
966 tensor is  $\text{def } \mathbf{u} = 0.5(\nabla \mathbf{u} + (\nabla \mathbf{u})^T)$ . Equation (10) implies that  $(1/\rho - 1/\rho_\infty) \nabla p_d$  is negligible.  
967 Physically this amounts to assuming that the baroclinic torque has a negligible contribution, relative  
968 to buoyancy, to the generation of vorticity. With this assumption a constant coefficient PDE for the  
969 pressure is formed by taking the divergence of the momentum equation [Eq.(9)]. This pressure PDE  
970 is solved in a computationally efficient and accurate manner using a direct solver. The baroclinic  
971 torque is then approximately restored using the pressure from the previous time step (McGrattan  
972 2004).

The influence of the grass fuel bed on the ambient wind flow is approximated by the drag term  $\mathbf{F}_D$  in Eq. (9). This drag term is present only in the first gas-phase grid cell above the bottom boundary, and is determined by

$$\mathbf{F}_D = \begin{cases} C_D \frac{3}{8} \beta_s \sigma_s \rho |\mathbf{u}| \mathbf{u} [1 - 0.9 m_{s,\text{pyr}}^f(t)], & 0 \leq m_{s,\text{pyr}}^f < 1, \\ C_D \frac{3}{8} \beta_s \sigma_s \rho |\mathbf{u}| \mathbf{u} [0.1], & m_{s,\text{pyr}}^f = 1, \end{cases} \quad (12)$$

where  $C_D \equiv 1$  is used which approximates a grass fuel element as a cylinder;  $\beta_s$  is the packing ratio of the solid fuel,  $\sigma_s$  is the surface to volume ratio of the solid fuel particles, and

$$m_{s,\text{pyr}}^f(t) = \frac{\int_0^t \dot{m}_{s,\text{pyr}}''(t') dt'}{m_{s,\text{pyr}}''(0)(1 - \chi_{\text{char}})}. \quad (13)$$

Here  $\dot{m}_{s,\text{pyr}}''$  is the rate of fuel gas generation due to pyrolysis of the vegetative solid,  $m_s''$  is the mass loading (mass per unit area) of the solid fuel bed, and  $\chi_{\text{char}}$  is the char fraction of the solid fuel. Equation (13) is the fraction of fuel that has undergone pyrolysis. Similar expressions for the terms not in the square brackets of Eq. (12) are used by Porterie et al. (2000) and Linn et al. (2002). The term in the square brackets approximates the weakening drag of the grass on the air flow as it burns away. For a given gas density and velocity field the drag of the fuel bed is reduced to 10% of its original value at the end of burning. The vegetative fuel variables in Eq. (12) are discussed more fully in Sec. A.2. This is a simple, first-step, model for representing the drag of the fuel bed. This approach is more explicit than the traditional boundary-layer meteorology method of treating the fuel as a zero-depth, constant friction surface of a particular roughness length based on the wind. It has the advantage of simplicity, a direct relationship to commonly measured fuel properties that are used in the fuel model, and varies with fuel consumption. How well it captures the influence of drag over a range of conditions is the subject of future research.

The computational grids used for the large fire simulations conducted here are too coarse to capture molecular transport physics. Instead an approximation to these subgrid processes using quantities resolved on the computational grid must be made. One approach to doing this is called large eddy simulations (LES), a variant of which is used here. Following Smagorinsky (1963) a subgrid scale model for the dynamic viscosity in the viscous stress tensor is used, where

$$\mu_{\text{LES}} = \rho(C\Delta)^2 \left( 2(\text{def } \mathbf{u}) \cdot (\text{def } \mathbf{u}) - \frac{2}{3}(\nabla \cdot \mathbf{u})^2 \right)^{\frac{1}{2}}. \quad (14)$$

Here  $C$  is an empirical constant (Smagorinsky constant),  $\Delta$  is a length on the order of the grid cell size, and the deformation term is related to the dissipation function (the rate at which kinetic energy is converted to thermal energy). The thermal conductivity and material diffusivity are related to turbulent viscosity  $\mu_{\text{LES}}$  by

$$\lambda_{\text{LES}} = \frac{\mu_{\text{LES}} c_{\text{p},\text{N}_2}}{\text{Pr}} \quad \text{and} \quad (\rho D)_{\text{LES}} = \frac{\mu_{\text{LES}}}{\text{Sc}}. \quad (15)$$

The Prandtl and Schmidt numbers,  $\text{Pr}$  and  $\text{Sc}$ , are constant. Values of  $C$ ,  $\text{Pr}$ , and  $\text{Sc}$  were obtained by comparing numerical simulations and laboratory experiments  $C = 0.2$ ,  $\text{Pr} = \text{Sc} = 0.5$  (McGrattan 2004). The equation for the conservation of species is

$$\rho \frac{\partial Y_i}{\partial t} + \rho \mathbf{u} \cdot \nabla Y_i = \nabla \cdot \{(\rho D)_{\text{LES}} \nabla Y_i\} + \dot{m}_i'''. \quad (16)$$

The equation of state is

$$p_o = \mathcal{R}\rho T \sum_i Y_i/M_i = \mathcal{R}\rho T/M. \quad (17)$$

The equation for conservation of energy is

$$\rho \frac{\partial h}{\partial t} + \rho \mathbf{u} \cdot \nabla h = \nabla \cdot (\lambda_{LES} \nabla T) + \nabla \cdot \left( \sum_i h_i (\rho D)_{LES} \nabla Y_i \right) - \nabla \cdot \dot{\mathbf{q}}_r'' + \frac{dp_o}{dt}. \quad (18)$$

Note that the WFDS simulations conducted here are not in a sealed enclosure, and therefore  $dp_o/dt = 0$ . The energy release associated with chemical reactions is not explicitly present but is accounted for by  $h$  (Rosner (2000), see their Eq.[20]). Here

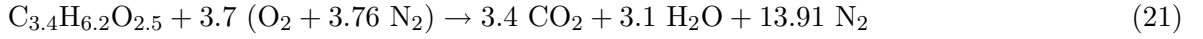
$$h(\mathbf{x}, t) = \sum_i Y_i(\mathbf{x}, t) h_i(T) \quad \text{and} \quad h_i(T) = h_i^o + \int_{T^o}^T c_{p,i}(T') dT' \quad (19)$$

986 are the enthalpy of the mixture and of species  $i$ , respectively. The temperature only dependence of  
987 the enthalpy of ideal gases is used. Note that  $c_p = \sum_i Y_i dh_i/dT$  is the mixture specific heat.

The molar heat of combustion for a given chemical reaction at constant pressure is

$$\Delta \bar{h}_c = - \sum_i \nu_i \bar{h}_i(T) = - \sum_i \nu_i h_i(T) M_i. \quad (20)$$

The simplified stoichiometric relation



is used to model the chemical reaction of air and fuel gases generated by wood pyrolysis (Ritchie et al. 1997). The mass consumption rate term for any of the species (except  $\text{N}_2$  which is chemically inactive) can be written in terms of a specific one. Thus in terms of the fuel mass consumption rate,

$$\dot{m}_i''' = r_i \dot{m}_F''' , \quad r_i = \frac{(\nu M)_i}{(\nu M)_F}, \quad \nu_F = -1, \quad \nu_{\text{O}_2} = -3.7, \quad \nu_{\text{CO}_2} = 3.4, \quad \nu_{\text{H}_2\text{O}} = 3.1. \quad (22)$$

With this expression the heat release per unit volume rate of the combustion process can be represented in terms of the heat of combustion:

$$\dot{Q}_c''' = - \sum_i h_i \dot{m}_i''' = - \frac{\dot{m}_F'''}{(\nu M)_F} \sum_i \nu_i h_i M_i = \frac{\dot{m}_F'''}{(\nu M)_F} \Delta \bar{h}_c = - \dot{m}_F''' \Delta h_c. \quad (23)$$

988 Here  $\Delta h_c = \Delta \bar{h}_c/M_F$  is the mass based heat of combustion and the fact that  $\nu_F \equiv -1$  is used.  
989

### 990 A.1.1 Divergence constraint

The divergence of the velocity is required in the conservation equation for total mass, Eq. (8). A general divergence constraint on the velocity can be derived by taking the material (or Lagrangian)

derivative of the equation of state

$$\dot{p}_o = \frac{\mathcal{R}T}{M} \frac{D\rho}{Dt} + \frac{\mathcal{R}\rho}{M} \frac{DT}{Dt} + \mathcal{R}\rho T \sum_i \frac{1}{M_i} \frac{DY_i}{Dt} \quad (24)$$

and using Eqs. (8), (16),  $DT/Dt$  from  $Dh/Dt$  where  $h$  is expressed in Eq. (19), and Eq. (18):

$$\begin{aligned} \nabla \cdot \mathbf{u} &= \frac{1}{\rho c_p T} \left( \nabla \cdot (\lambda_{LES} \nabla T) + \sum_i (\rho D)_{LES} \nabla Y_i \cdot \nabla h_i - \nabla \cdot \dot{\mathbf{q}}_r'' \right) \\ &\quad + \frac{1}{\rho} \sum_i \frac{M}{M_i} \nabla \cdot \{(\rho D)_{LES} \nabla Y_i\} + \frac{1}{\rho} \sum_i \left( \frac{M}{M_i} - \frac{h_i}{c_p T} \right) \dot{m}_i''' . \end{aligned} \quad (25)$$

A similar expression for the divergence constraint was used in simulations by Bell et al. (2000) of vortex flame interaction neglecting thermal radiation. Equation (25) can be simplified using the assumption that the ratio of specific heats,  $\gamma$ , for each species is equal to the value for diatomic gases, or

$$\gamma_i = \frac{\bar{c}_{p,i}}{\bar{c}_{v,i}} = \frac{c_{p,i}}{c_{v,i}} = \gamma = 7/5 \quad \Rightarrow \quad \bar{c}_{p,i} = \bar{c}_p, \quad \bar{c}_{v,i} = \bar{c}_v \quad \text{constant.} \quad (26)$$

The basis for this assumption is that nitrogen is the dominant species in the gas mixture. The implication that the molar specific heats are constant follows from  $\bar{c}_{p,i} - \bar{c}_{v,i} = \mathcal{R}$ . With this assumption the divergence constraint can be written

$$\begin{aligned} \nabla \cdot \mathbf{u} &= \frac{1}{\rho c_p T} \left( \nabla \cdot (\lambda_{LES} \nabla T) + \sum_i c_{p,i} \nabla \cdot \{T(\rho D)_{LES} \nabla Y_i\} - \nabla \cdot \dot{\mathbf{q}}_r'' \right) \\ &\quad + \frac{1}{\rho} \sum_i \left( \frac{M}{M_i} - \frac{h_i}{c_p T} \right) \dot{m}_i''' , \end{aligned} \quad (27)$$

where the relation

$$c_{p,i} = \frac{\mathcal{R}}{M_i} \frac{\gamma}{\gamma - 1} = \text{constant}, \quad c_p = \sum_i Y_i c_{p,i} = \frac{\mathcal{R}}{M} \frac{\gamma}{\gamma - 1} \quad \Rightarrow \quad \frac{M}{M_i} = \frac{c_{p,i}}{c_p} \quad (28)$$

is used to combine the two diffusion terms in Eq. (25). Note that the specific heats are independent of temperature but do depend on the molecular weight of the gas species.

In each form of the divergence constraint the mass consumption terms are, using Eqs. (22) and (23),

$$\frac{1}{\rho} \sum_i \left( \frac{M}{M_i} - \frac{h_i}{c_p T} \right) \dot{m}_i''' = \frac{1}{\rho} \left( \frac{M \sum_i \nu_i}{\nu_F M_F} - \frac{\Delta h_c}{c_p T} \right) \dot{m}_F''' = \frac{M \sum_i \nu_i}{\rho \nu_F M_F} \dot{m}_F''' + \frac{1}{\rho c_p T} \dot{Q}_c''', \quad (29)$$

where  $\dot{Q}_c'''$  is the chemical heat release per unit volume given in Eq. (23). An order of magnitude analysis shows that the first term on the right-hand-side can be neglected for the complex hydrocarbon fuel gases and is not included in the numerical implementation of WFDS. To determine the the chemical heat release rate per unit volume, Eq. (23), the combustion process must be modeled. This model provides the fuel mass consumption term  $\dot{m}_F'''$  and is discussed next.

1002 **A.1.2 Mixture fraction based combustion model**

Even when available, models of detailed chemical kinetics are too computationally expensive to implement in simulations of the scale we are interested in. Instead, we adopt the commonly used mixture fraction based fast chemistry or flame sheet model (Bilger 1980). In this model it is assumed that the time scale of chemical reactions is much shorter than that of mixing (i.e., “mixed is burnt”). The mixture fraction,  $Z$ , is defined as:

$$Z \equiv \frac{r_{O_2} Y_F - (Y_{O_2} - Y_{O_2}^\infty)}{r_{O_2} Y_F^\infty + Y_{O_2}^\infty}, \quad 0 \leq Z \leq 1, \quad (30)$$

where the dependence of  $Y_F$  and  $Y_{O_2}$  on  $Z$  can be easily determined by applying the flame sheet assumption,  $Y_F Y_{O_2} = 0$ . Here  $Y_F^\infty$  is the fuel mass fraction in the fuel stream,  $Y_{O_2}^\infty$  is the oxygen mass fraction in the ambient atmosphere, and  $r_{O_2}$  is defined in Eq. (22). If the fuel and oxygen are in stoichiometric proportions,  $r_{O_2} Y_F = Y_{O_2}$ , and they are each completely consumed by the chemical reaction where

$$Z = Z_{st} = Y_{O_2}^\infty / (r_{O_2} Y_F^\infty - Y_{O_2}^\infty) \quad (31)$$

1003 is the location of the flame sheet or combustion zone.

1004 With this combustion model the chemical reaction occurs solely as the result of fuel and oxygen  
1005 mixing in stoichiometric proportion and so is independent of temperature. In reality chemical  
1006 reactions are dependent on temperature. However, the computational grids used here are much too  
1007 coarse ( $\mathcal{O}(1 \text{ m})$ ) to resolve the combustion zone ( $\mathcal{O}(1 \text{ mm})$ ). Thus, in a WFDS simulation the heat  
1008 released by the combustion process is deposited in computational grid cell volumes that are much  
1009 larger than volumes occupied by actual combustion zones. For this reason flame temperatures can  
1010 not be reached and Arrhenius type reaction models that require a resolved temperature field can  
1011 not be directly used. An alternative is presented below.

The conservation equation for  $Z$  is obtained by combining the conservation equations for  $Y_F$  and  $Y_{O_2}$  according to Eq. (30) and using Eq. (22):

$$\frac{\partial \rho Z}{\partial t} + \mathbf{u} \cdot \nabla(\rho Z) = -\rho Z \nabla \cdot \mathbf{u} + \nabla \cdot \{(\rho D)_{LES} \nabla Z\}. \quad (32)$$

With this equation, Eq. (22), and zero boundary conditions (at  $Z = 0, 1$ ) the dependence of  $Y_{CO_2}$  and  $Y_{H_2O}$  on  $Z$  can be determined. The divergence constraint is

$$\nabla \cdot \mathbf{u} = \frac{1}{\rho c_p T} \left( \nabla \cdot (\lambda_{LES} \nabla T) - \sum_i Y'_i c_{p,i} \nabla \cdot (T \rho D \nabla Z) - \nabla \cdot \dot{\mathbf{q}}''_r + \dot{Q}_c''' \right), \quad (33)$$

where Eq. (23) is used for  $\dot{Q}_c'''$ . In the context of the mixture fraction combustion model, the fuel mass consumption term is

$$\dot{m}_F''' = Y'_F \nabla \cdot (\rho D \nabla Z) - \nabla \cdot (Y'_F \rho D \nabla Z) = -Y''_F \rho D |\nabla Z|^2. \quad (34)$$

The numerical implementation of this expression is problematic because  $Y'_F = dY_F/dZ$  is discontinuous. Instead an expression for the mass consumption per unit area of flame sheet, which can

be derived via a line integral through the flame sheet, is used. For example, for oxygen

$$\dot{m}_{O_2}'' = -Y_{O_2}'|^{Z \leq Z_{st}}(\rho D|\nabla Z|)|^{Z=Z_{st}} = \frac{(\nu M)_{O_2}}{(\nu M)_F} \dot{m}_F'', \quad (35)$$

which implies, using Eq. (23), that the local chemical heat release per unit area of flame sheet is

$$\dot{Q}_c'' = -\Delta h_c \frac{(\nu M)_F}{(\nu M)_{O_2}} Y_O'|^{Z \leq Z_{st}}(\rho D|\nabla Z|)|^{Z=Z_{st}}. \quad (36)$$

This expression is used to determine  $\dot{Q}_c'''$  at locations corresponding to the flame sheet. The value of the heat of combustion per kg of gaseous fuel is  $\Delta h_c = 15600 \text{ kJ kg}^{-1}$ . This is a representative value for a range of grasses reported in Hough (1969) and Susott (1982).

It can be shown that the summation of Eq. (36) along the flame sheet is consistent with the total heat released by the complete combustion of the fuel gas generated by pyrolysis (i.e., arising from the fuel bed) (McGrattan 2004). This very important constraint ensures that the convective and radiative heat transported to the vegetative fuel and to surrounding soot laden gases are consistently coupled to the pyrolysis of the solid fuel. The assumption of complete consumption of the fuel gases is valid only if a sufficient amount of oxygen is present in the volume surrounding the fire. For fire plumes in unbounded domains this is a reasonable assumption. Similar considerations are required for radiative emission as discussed below.

### A.1.3 Thermal radiation transport

The radiation transport equation (RTE) for an absorbing-emitting, non-scattering gas is

$$\hat{s} \cdot \nabla I_\lambda(\mathbf{x}, \hat{s}) = \kappa_\lambda(\mathbf{x})[I_{b,\lambda}(\mathbf{x}) - I_\lambda(\mathbf{x}, \hat{s})]. \quad (37)$$

Note that the dependence of the intensity,  $I$ , on the frequency of the radiation,  $\lambda$ , is due to the spectral (frequency) dependence of the absorption coefficient  $\kappa_\lambda$ . However, fires from vegetative fuels are heavily soot laden. Since the radiation spectrum of soot is continuous, it is assumed that the gas behaves as a spectrally independent or gray medium. This results in a significant reduction in computational expense. The spectral dependence is therefore combined into one absorption coefficient,  $\kappa$ , and the emission term is given by the blackbody radiation intensity

$$I_b(\mathbf{x}) = \sigma T^4(\mathbf{x})/\pi. \quad (38)$$

A table containing the values of  $\kappa$  as function of mixture fraction and temperature for a given mixture of participating gaseous species ( $H_2O$ ,  $CO_2$ ) and soot particulate is computed before the simulation begins. A soot evolution model is not used. Instead, the mass of soot generated locally is an assumed fraction,  $\chi_s$ , of the mass of fuel gas consumed by the combustion process. In the WFDS simulations reported here,  $\chi_s = 0.02$  is used. Values of  $\chi_s$  for Douglas fir range from less than 0.01 to 0.025 under flaming conditions (Bankston et al. 1981).

Integrating the spectrally independent form of Eq. (37) over all solid angles gives the equation for conservation of radiant energy,

$$\nabla \cdot \dot{\mathbf{q}}_r''(\mathbf{x}) = \kappa(\mathbf{x})[4\pi I_b(\mathbf{x}) - U(\mathbf{x})], \quad (39)$$

where  $U$  is the integrated radiation intensity. This equation states that the net radiant energy lost in a unit volume per unit time is the difference between the emitted and absorbed radiant energy.

1032 The divergence of the radiation flux in Eq. (39) is required in the energy equation, Eq. (18), and  
 1033 in the divergence of the velocity, which is used in the numerical solution procedure, Eq. (33).

As was discussed above, the spatial resolution in the large scale WFDS simulations conducted here is insufficient to resolve the combustion zone. As a result, local gas temperatures on the computational grid in the flame zone region are significantly lower than actual flame temperatures. This requires special treatment of the radiation emission term  $\kappa I_b$  in the flame region since it depends on the fourth power of the local temperature. In regions where the temperature is lower and spatial gradients are not so under predicted, the numerical temperatures are more realistic. For this reason the emission term is modeled as

$$\kappa I_b = \begin{cases} \kappa\sigma T^4/\pi, & \text{outside the flame zone} \\ \chi_r \dot{Q}_c'''', & \text{inside the flame zone} \end{cases} \quad (40)$$

1034 where  $\chi_r$  is the fraction of the chemical heat release rate per unit volume that is radiated to the  
 1035 local volume surrounding the flame region. Note that some of this radiation will be absorbed by the  
 1036 surrounding soot. As a result, for the fire as a whole, the fraction of chemical heat release radiated  
 1037 to a location outside the smoke plume will be smaller than the local value. For hydrocarbon pool  
 1038 fires the local value is  $\chi_r \cong 0.30$  to  $0.35$  while the global value is less,  $0.10$  (Koseki and Mulhooand  
 1039 1991). In wood cribs  $\chi_r \cong 0.20$  to  $0.40$  (Quintiere 1997). The value used in the simulations is  
 1040  $\chi_r = 0.35$ .

1041 An earlier implementation of the simulation code used the P1 approximation form of the RTE (Baum  
 1042 and Mell 1998). The P1 approximation was also used by Porterie et al. (1998) in the first stages of  
 1043 their two-dimensional model for fire spread through a pine needle bed and by Grishin (1996). The  
 1044 P1 approximation is accurate only when the absorption coefficient of the gases is sufficiently large.  
 1045 Since radiation transport through air, which is optically thin, to the vegetative fuel is an important  
 1046 contribution to the net heat flux on the vegetation ahead of the fire, the P1 approximation is not  
 1047 appropriate in general. For this reason a finite volume method based on that of Raithby and Chui  
 1048 (1990) is used to solve the gray gas form of Eq. (37). It requires approximately 20% of the total  
 1049 CPU time. The spatial discretization of the RTE is the same as that used in the other gas phase  
 1050 conservation equations. The details of the implementation of this approach, including boundary  
 1051 conditions for open and solid boundaries, are in McGrattan (2004).

1052 The set of gas phase conservation equations solved in the simulation consists of the conservation  
 1053 of total mass Eq. (8), the momentum Eq. (9), the mixture fraction Eq. (32), the divergence of the  
 1054 velocity Eq. (33), and the gray gas form of Eq. (37). The equation of state, Eq. (17), is used to  
 1055 obtain the temperature field. In addition, an equation for the pressure field, obtained by taking  
 1056 the divergence of the momentum equation, is solved using a fast direct solver.

## 1057 A.2 Approach for modeling the solid fuel

1058 The decomposition of a vegetative fuel subjected to a sufficiently high heat flux is a complex  
 1059 process occurring through two general steps: evaporation of moisture and then pyrolysis of the  
 1060 solid. During pyrolysis, chemical decomposition occurs forming char and volatiles that pass out of  
 1061 the solid fuel into the surrounding gas. The above processes are all endothermic. The exothermic  
 1062 process of char oxidation can occur if oxygen is present at a sufficiently hot char surface. If the  
 1063 combustible pyrolysis volatiles mix with enough ambient oxygen at high enough temperatures, then  
 1064 flame ignition occurs. As discussed in the previous section, the combustion model used here assumes  
 1065 that ignition occurs when fuel gas and oxygen mix in stoichiometric proportion, independent of the  
 1066 gas temperature.

1067 Many models of the thermal and mass transport and the kinetics of chemical decomposition for

wood subjected to a prescribed heat flux have been developed. Mostly these models are thermally thick and vary according to how they approximate the anisotropy of the wood material, moisture content, wood constituents, physics of heat and mass transport, and the chemical kinetics of pyrolysis and char oxidation. Reviews of these models can be found in Di Blasi (1993) and Atreya (1983). More recently three-dimensional models have been used (e.g., Yuen et al. (1997)). Numerous thermally thin models for the pyrolysis of cellulose and subsequent flame spread also exist (e.g., Mell et al. (2000); Porterie et al. (2000)).

In all of the above studies either the external heat flux was prescribed or the flame was simulated on a sufficiently fine computational grid that the flame's temperature/structure was well resolved. In the modeling approach taken here the grassland fuel bed is assumed to be comprised of uniformly distributed, non-scattering, perfectly absorbing, thermally thin fuel particles of density  $\rho_s$  and surface-to-volume ratio  $\sigma_s$ . The thermally thin assumption is commonly used in fire models involving fine wildland fuels (grass and foliage of shrubs and trees) (Rothermel 1972). Note that an emissivity of 0.9 is characteristic of wildland vegetation (Jarvis et al. 1976) so the assumption that a fuel element is a perfect absorber is a reasonable one. The bulk density of the fuel bed is  $\rho_{sb}$  and the fraction of the fuel bed volume occupied by the fuel particles, or packing ratio, is  $\beta = \rho_{sb}/\rho_s$ . The temperature evolution equation of the solid fuel in a vegetative fuel bed with these properties is (following Morvan and Dupuy (2004))

$$\beta_s \rho_s c_{p,s} \frac{\partial}{\partial t} T_s(x, y, z, t) = -\nabla \cdot \dot{q}_{sr}'' - \nabla \cdot \dot{q}_{sc}'' - \dot{Q}_{s,vap}''' - \dot{Q}_{s,kin}'''. \quad (41)$$

Here  $\nabla \cdot \dot{q}_{sr}''$  and  $\nabla \cdot \dot{q}_{sc}''$  are the divergences of the thermal radiation (spectrally integrated) and conductive heat fluxes on the solid fuel elements within the bulk vegetative fuel bed;  $\dot{Q}_{s,vap}'''$  contains the endothermic effect of vaporization of moisture;  $\dot{Q}_{s,kin}'''$  contains the contribution of heats (endothermic and exothermic) associated with the thermal degradation of the solid (e.g., pyrolysis, char oxidation);  $c_{p,s}$  is the specific heat of the fuel particle, which can contain moisture. This equation, without  $\dot{Q}_{s,kin}'''$ , was also used by Albini (1985, 1986).

The radiative heat flux can be found by solving the thermal radiation heat transfer equation, Eq. (37), (or an approximation to it, as is done below) in the fuel bed. This requires the absorption coefficient,  $\kappa_s$ , of the bulk fuel bed which can be related to field measurements of the average surface-to-volume ratio and the packing ratio of the fuel particles (NAS 1961),

$$\kappa_s = \frac{1}{4} \beta_s \sigma_s = \frac{1}{4} \frac{w_s \sigma_s}{\rho_s h_s}, \quad (42)$$

where  $w_s$  is the fuel bed loading and  $h_s$  is the fuel bed height. This expression for the absorption coefficient has been used in other fire spread models (Albini 1985, 1986; De Mestre et al. 1989; Morvan and Dupuy 2001, 2004) and has been experimentally validated for vegetative fuels (Butler 1993).

The bulk conductive heat flux term in Eq.(41) is approximated by the volume-averaged sum of the local flux on the surface of individual fuel particles. For a representative volume  $V$  containing  $N_p$  fuel particles

$$\nabla \cdot \dot{q}_{sc}'' \cong \frac{\sum_{i=1}^N \int \dot{q}_{sc,p}'' \cdot \hat{n} dS_{p,i}}{V} \cong \frac{\dot{q}_{sc,p}'' N_p S_p}{V} = \frac{N_p S_p}{N_p V_p} \frac{N_p V_p}{V} \dot{q}_{sc,p}'' = \sigma_s \beta_s \dot{q}_{sc,p}'', \quad (43)$$

where  $S_p$ ,  $V_p$  and  $\dot{q}_{sc,p}''$  are the surface area, volume, and net surface conductive heat flux associated with a representative fuel particle, respectively. The conductive heat flux is assumed to be uniform

1087 across the surface of the fuel particle which is consistent with the assumption that the particle is  
 1088 thermally thin and surrounded by gas of constant temperature  $T_g$ .

1089 Model Eqs. (41), (42) and (43) have been used to predict heat transfer in two-dimensional  
 1090 vegetative fuel beds by Albini (1986) to obtain steady-state fire spread rates ( $\dot{Q}_{s,\text{kin}}''' \equiv 0$ ). These  
 1091 equations along with a model for thermal degradation (to determine  $\dot{Q}_{s,\text{kin}}'''$ ) have also been used in  
 1092 the two-dimensional simulation of Morvan and Dupuy (2004) (and their earlier work). Morvan and  
 1093 Dupuy solve the governing equations for the solid fuel and gas phase on the same computational  
 1094 grid with a cell size of 10 mm in the pyrolysis zone. This is not possible in the present study since  
 1095 the gas phase cells are  $\mathcal{O}(1)$  m. Instead, the fuel bed is given its own uniform computational grid  
 1096 on which Eq. (41) is solved (see Fig. 20). Within the gas phase computational grid the fuel bed  
 1097 is present as a momentum drag only. Thermal and mass flux interaction of the gas and vegetative  
 1098 grids occurs at the gas/vegetation boundary,  $(x_\Gamma, y_\Gamma, 0)$  in gas phase coordinates. The temperature  
 1099 of the solid fuel in the vegetative fuel bed is assumed to depend on the vertical coordinate only,  
 1100  $T_s(x_s, y_s, z_s, t) = T_s(x_\Gamma, y_\Gamma, z_s, t)$  beneath each gas phase grid cell along the gas/vegetation boundary.  
 1101 The resolution of the grid used for the vegetation is  $\Delta z_s \leq (3\kappa_s)^{-1}$ , is based on the optical depth of  
 1102 the fuel bed,  $\kappa_s^{-1}$  (Morvan and Dupuy 2001). Initially, the number of layers spanning the height  
 1103 of the fuel bed is  $N_L = h_s \Delta z_s^{-1}$ . The grassland fuel bed is assumed to burn from the top down  
 1104 causing the total number of layers to decrease with time. It should be noted that this assumption  
 1105 of top down burning is more consistent with field observations of head fires, which spread with the  
 1106 ambient wind, as opposed to fire spread either into the wind (backing fire) or across the ambient  
 1107 wind (flanking fire). As the fuel bed burns away, the term in the square brackets in Eq. (12)  
 1108 decreases in magnitude (i.e., the influence of drag decreases).

1109 It is assumed that radiation within the fuel bed is spectrally independent and travels in only  
 1110 two directions, either downward or upward. This is commonly called the forward-reverse radiation  
 1111 transfer model (Ozisk 1973; Mell and Lawson 2000). The net radiative flux within the fuel bed has  
 1112 contributions from the downward radiative flux due to the fire, incident on the top of fuel bed ( $\dot{q}_{sr,i}''^+$ ,  
 1113 see Fig. 20) and from the radiative flux due to local self emission (integrals in Eq. (44) below).  
 1114 With these assumptions the net radiative flux at a nondimensional distance  $\eta_s = \kappa_s z_s$  from the top  
 1115 of the fuel bed is:

$$\begin{aligned}\dot{q}_{sr}''(\eta_s) &= \dot{q}_r''^+ + \dot{q}_r''^- \\ &= \dot{q}_{sr,i}''^+ \exp(-[\eta_{s,h} - \eta_s]) + \sigma \int_{\eta_s}^{\eta_{s,h}} T_s^4 \exp(-[\eta'_s - \eta_s]) d\eta'_s \\ &\quad - \dot{q}_{sr,i}''^- \exp(-\eta_s) - \sigma \int_0^{\eta_s} T_s^4 \exp(-[\eta_s - \eta'_s]) d\eta'_s,\end{aligned}\quad (44)$$

1116 where  $\eta_{s,h} = \kappa_s h_s$ . The net radiative flux on the bottom boundary of the fuel bed is assumed to  
 1117 be zero (this defines  $\dot{q}_{sr,i}''^+$ ). This radiation boundary assumption was also made by Albini (1986)  
 1118 for fire spread through surface fuels where the bottom boundary is soil. The radiation transfer  
 1119 computation in the gas phase provides  $\dot{q}_{sr,i}''^-$ .

1120 With the above assumptions, integrating Eq. (41) over a control volume  $dx_\Gamma dy_\Gamma dz_s$  centered at  
 1121  $z_{s,n}$ , the center of the  $n$ th cell in the solid fuel's computational grid (see Fig. 20), gives

$$\begin{aligned}[m_s'' c_{p,s} \frac{\partial T_s}{\partial t}]_n &= -[\dot{q}_{sr}''(\eta_s^+) \cdot \hat{n}^+ + \dot{q}_{sr}''(\eta_s^-) \cdot \hat{n}^-]_n - [\sigma_s \beta_s \dot{q}_{sc,p}'' + \dot{Q}_{s,vap}''' + \dot{Q}_{s,kin}''']_n \Delta z_s \\ &= [\dot{q}_{s,\text{net}}'']_n - [\dot{Q}_{s,vap}''' + \dot{Q}_{s,kin}''']_n \Delta z_s.\end{aligned}\quad (45)$$

Here

$$[\dot{q}_{\text{sr},\text{net}}'']_n = -\dot{\mathbf{q}}_{\text{sr}}''(\eta_{s,n}^+) \cdot \hat{\mathbf{n}}^+ - \dot{\mathbf{q}}_{\text{sr}}''(\eta_{s,n}^-) \cdot \hat{\mathbf{n}}^- - \sigma_s \beta_s \dot{q}_{\text{sc,p}}'' \Delta z_s = \dot{q}_{\text{sr},\text{net},n}'' + \dot{q}_{\text{sc},\text{net},n}'' \quad (46)$$

is the net heat flux on the bulk solid fuel;  $\eta_{s,n}^-$  and  $\eta_{s,n}^+$  are the locations of the lower and upper horizontal faces, respectively, of the  $n$ th grid cell; and  $\hat{\mathbf{n}}^+$ ,  $\hat{\mathbf{n}}^-$  are the outward facing normals on these faces. All other quantities are cell-centered. It is assumed that the rate at which thermal energy is stored in the control volume, the right-hand-side of Eq. (45), and the heat sinks and sources associated with vaporization and thermal degradation, are constant throughout the cell volume. Values of  $\dot{q}_{\text{sr},\text{net},1}''$  and  $\dot{q}_{\text{sc},\text{net},1}''$  versus time were plotted previously on Fig. 2. In general, the solid fuel mass per area in grid cell  $n$ ,  $[m_s'']_n$ , is composed of dry virgin vegetative fuel and moisture  $m_s'' = m_{s,v}'' + m_{s,m}''$ . Initially  $[m_{s,v}''(t=0)]_n = w_s \Delta z_s / h_s$  and  $[m_{s,m}''(t=0)]_n = M[m_{s,v}''(t=0)]_n$  where  $M$  is the moisture fraction.  $M$  is defined to be the mass of initial moisture in a fuel particle divided by its mass when dry. The specific heat of the fuel particle has, in general, contributions from moisture and vegetation (Porterie et al. 1998):

$$c_{p,s} = \frac{m_{s,v}'' c_{p,v} + m_{s,m}'' c_{p,m}}{m_s''}, \quad (47)$$

where  $c_{p,v}$  (which depends on  $T_s$ ) and  $c_{p,m}$  are given in Table 1.

The conductive heat flux on the surface of a fuel particle,  $\dot{q}_{\text{sc,p}}''$ , in Eq. (46) is determined using a convective heat transfer coefficient,  $h_c$ , for a vertical cylinder (Holman 1981), and is defined by

$$\dot{q}_{\text{sc,p}}'' = h_c(T_s - T_g), \quad h_c = 1.42(|T_s - T_g|/\Delta z_s)^{1/4}. \quad (48)$$

$T_g$  is the temperature in the bottom gas phase grid cell bordering the fuel bed, and  $\Delta z_s$  is the length of the cylinder in the  $n$ th fuel layer.

The temperature equation, Eq. (45), for the fuel bed is solved assuming a two stage endothermic decomposition process (water evaporation followed by solid fuel pyrolysis). At this stage in the model development char oxidation is not accounted for, and  $\dot{Q}_{s,\text{kin}}''' = \dot{Q}_{s,\text{pyr}}'''$ . In a given fuel layer the virgin fuel dries and then undergoes pyrolysis until the solid mass remaining equals  $\chi_{\text{char}} w_s / N_L$  where  $\chi_{\text{char}}$  is the char fraction of the solid fuel and  $N_L$  equals the original number of layers in the fuel model (see Fig. 20). A char mass fraction of  $\chi_{\text{char}} = 0.2$  was used based on measurements of grass fuels by Susott (1982).

Moisture is removed in a manner similar to previous models (Albini 1985; De Mestre et al. 1989; Margeri and Sero-Guillaume 2002; Morvan and Dupuy 2004). The temperature of the vegetative fuel bed evolves according to Eq. (45). Once  $T_s$  reaches boiling temperature,  $T_b$ , it is assumed that drying requires all of the available heat so that  $T_s = T_b$  until all the moisture has evaporated. With these assumptions the drying stage of fuel decomposition is modeled as:

$$\begin{aligned} \dot{Q}_{s,\text{vap}}''' &= \dot{m}_{s,m}'' \Delta h_{\text{vap}} / \Delta z_s, \\ \dot{m}_{s,m}'' &= \begin{cases} 0, & T_s < T_b, \\ \dot{q}_{s,\text{net}}'' / \Delta h_{\text{vap}}, & T_s = T_b, \quad m_{s,m}'' > 0, \quad \dot{q}_{s,\text{net}}'' > 0, \end{cases} \\ \dot{Q}_{s,\text{pyr}}''' &= 0. \end{aligned} \quad (49)$$

After all the moisture is boiled off, the temperature of the fuel bed is free to change according to Eq. (45) with  $m_{s,m}'' = 0$ . With a net influx of heat,  $T_s$  continues to rise, eventually reaching a point  $T_s = T_{\text{pyr}}$ , where pyrolysis begins and  $\dot{Q}_{s,\text{pyr}}''' \neq 0$ .

This is as far as the physics-based fire/fuel spread models such as Albini (1985) and De Mestre

et al. (1989) go since the incident heat flux from the fire is assumed, allowing the steady-state fire spread rate to be determined based on how long it takes  $T_s$  to reach  $T_{\text{pyr}}$ . In our case, however, the computer simulation supplies the time-dependent heat flux based on the behavior of the simulated fire, which drives the pyrolysis of the solid fuel and determines  $\dot{m}_{\text{s,pyr}}''$ , the rate at which fuel gas is generated. Physics-based computer simulation approaches of fire spread in vegetative fuels that have well resolved gas phase flames, such as Porterie et al. (1998) and Morvan and Dupuy (2001), use temperature dependent Arrhenius kinetics for pyrolysis and char oxidation. More recently Morvan and Dupuy (2004) found that a simple temperature dependent pyrolysis mass loss rate was as accurate as a more complicated Arrhenius expression. The model for solid fuel thermal degradation used here uses the temperature dependent mass loss rate expression in Morvan and Dupuy (2004). This pyrolysis model was based on thermogravimetric analysis of number of vegetation species (Dimitrakipoulos 2001; Moro 1997). Since char oxidation is not modeled the smoldering or glowing combustion in the grass, after the fire front has passed, is not present. Thus, in the simulations reported here the pyrolysis stage of decomposition is (Morvan and Dupuy 2004):

$$\begin{aligned}
 \dot{Q}_{\text{s,vap}}''' &= 0, \\
 \dot{Q}_{\text{s,pyr}}''' &= \dot{m}_{\text{s,pyr}}'' \Delta h_{\text{pyr}} / \Delta z_s \\
 \dot{m}_{\text{s,pyr}}'' &= \begin{cases} 0, & T_s < 127 \text{ C}, \\ (\dot{q}_{\text{s,net}}'' / \Delta h_{\text{pyr}}) (T_s - 127) / 100, & 127 \text{ C} \leq T_s \leq 227 \text{ C}, \dot{q}_{\text{s,net}}'' > 0, \\ & \text{and } m_{\text{s}}'' > \chi_{\text{char}} w_{\text{s}}. \end{cases} \quad (50)
 \end{aligned}$$

The heat of pyrolysis,  $\Delta h_{\text{pyr}}$ , is 416 kJ kg<sup>-1</sup> (Morvan and Dupuy 2004). When the mass loss, in the  $n^{\text{th}}$  solid phase cell, is such that  $m_{\text{s},n}'' = \chi_{\text{char}} w_{\text{s}} / N_{\text{L}} = m_{\text{char},n}'''$  then the fuel in that layer is assumed to be consumed and it is removed from the solid fuel model.

1158 **B Nomenclature**

<u>Variable</u>	<u>Units</u>	<u>Description</u>
$c_p$	$\text{kJ kg}^{-1}\text{K}^{-1}$	specific heat at constant pressure
$c_{p,i}$	$\text{kJ kg}^{-1}\text{K}^{-1}$	specific heat of species $i$ at constant pressure
$\bar{c}_{v,i}$	$\text{kJ/kmole}\cdot\text{K}$	molar specific heat of species $i$ at constant volume
$D$	$\text{m}^2 \text{s}^{-1}$	mass diffusivity
$d$	$\text{m}$	depth of head fire
$d_{ig}$	$\text{m}$	depth of ignition fire-line
$\mathbf{g}$	$\text{m/s}^2$	ambient acceleration vector
$\mathcal{H}$	$\text{m}^2/\text{s}^2$	modified pressure term in momentum equation
$h = \sum_i Y_i h_i$	$\text{kJ/kg}$	mixture enthalpy
$h_b$	$\text{m}$	height of bulk vegetative fuel
$h_i$	$\text{kJ/kg}$	specific enthalpy of species $i$
$\bar{h}_i = h_i M_i$	$\text{kJ/kmole}$	molar specific enthalpy of species $i$
$h_s$	$\text{m}$	height of solid fuel
$\mathbf{I}$	-	identity matrix
$I_\lambda(\mathbf{x}, \hat{\mathbf{s}})$	$\text{W}\cdot\text{MHz}/\text{m}^2 \cdot \text{sr}$	spectral radiation intensity
$I_b(\mathbf{x}, \hat{\mathbf{s}})$	$\text{W}\cdot\text{MHz}/\text{m}^2 \cdot \text{sr}$	blackbody radiation intensity
$L_{ig}$	$\text{m}$	length of ignition line
$\dot{m}_{s,\text{pyr}}''$	$\text{kg/m}^2\cdot\text{s}$	mass flux of fuel gas due to pyrolysis of vegetative solid fuel
$\dot{m}_i'''$	$\text{kg/s} \cdot \text{m}^3$	chemical mass consumption of gas species $i$
$s, \dot{m}_{m,e}''$	$\text{kg/m}^2\cdot\text{s}$	mass flux of water vapor from vegetative fuel element during drying
$M$	-	fuel moisture content as fraction of oven dried fuel mass
$M_i$	$\text{kg/kmole}$	molecular weight of gas species $i$
$M = (\sum_i Y_i/M_i)^{-1}$	$\text{kg/kmole}$	average molecular weight of gas mixture
$\hat{\mathbf{n}}$	-	unit normal vector
$\dot{Q}_c'''$	$\text{kW/m}^3$	heat release rate per unit volume due to chemical reactions
$p_d$	$\text{Pa}$	dynamic pressure
$p_o$	$\text{Pa}$	a thermodynamic pressure
$\mathcal{R} = 8.314$	$\text{kJ kmole}^{-1}\text{K}^{-1}$	universal gas constant
$R_o$	$\text{m s}^{-1}$	experimentally observed head fire spread rate
$R_s$	$\text{m s}^{-1}$	empirically derived potential quasi-steady head fire spread rate
$\dot{q}''$	$\text{kW m}^{-2}$	magnitude of heat flux
$\dot{\mathbf{q}}''$	$\text{kW m}^{-2}$	heat flux vector
$\hat{\mathbf{s}}$	-	unit vector in direction of radiation intensity
$T$	$^\circ\text{C}$	temperature
$\mathbf{u}$	$\text{m s}^{-1}$	velocity vector
$w_s$	$\text{kg m}^{-2}$	vegetative fuel loading
$U$	$\text{W m}^{-2}$	integrated radiation intensity
$U_2$	$\text{m s}^{-1}$	wind speed in direction of spread at 2 m above ground
$\mathbf{x}$	$\text{m}$	position vector
$W$	$\text{m}$	width of head fire

$Y_i = \rho_i/\rho$	-	local mass fraction of species $i$
$Y_F^\infty$	-	mass fraction of fuel in fuel stream
$Y_{O_2}^\infty$	-	mass fraction of oxygen in oxidant
$Z$	-	local mixture fraction
$Z_{st}$	-	stoichiometric value of the mixture fraction
$\beta$	-	packing ratio, $\rho_b/\rho_e$
$\gamma_i = c_{p,i}/c_{v,i}$	-	ratio of species $i$ specific heats
$\Delta\bar{h}_c$	kJ/kmole	molar based heat of combustion
$\eta_s = \kappa_s z_s$	-	nondimensional distance from top of fuel bed
$\Delta h_c$	kJ/kg	mass based heat of combustion
$\Delta h_{vap}$	kJ/kg	heat of vaporization of water
$\Delta h_p$	kJ/kg	heat of pyrolysis of vegetative fuel
$\Delta x, \Delta y, \Delta z$	m	length of computational cell in $x, y, z$ directions
$\sigma_s$	$m^{-1}$	surface-to-volume ratio of fuel elements
$\sigma$	$5.67 \times 10^{-11} \text{ kW m}^{-2} \text{ K}^{-4}$	Stefan-Boltzmann constant
$\lambda$	$\mu\text{m}$	wavelength of radiation, or
$\lambda$	W/m·K	thermal conductivity of the gaseous mixture
$\mu$	kg / m· s	dynamic viscosity of the gaseous mixture
$\nu_i$	-	stoichiometric coefficient of species $i$
$\rho$	kg/m <sup>3</sup>	total density of gas
$\rho_{sb}$	kg/m <sup>3</sup>	bulk density of solid fuel
$\rho_s$	kg/m <sup>3</sup>	fuel particle density
$\tau$	kg/m · s <sup>2</sup>	viscous stress tensor
$\chi_{\text{char}}$	-	fraction of virgin solid fuel converted to char
$\chi_r$	-	fraction of local chemical heat release radiated to surroundings
$\chi_s$	-	fraction of consumed fuel mass converted to soot

1160

Subscripts

a	ambient
b	boiling or bulk vegetative fuel quantity
c	convective
i	incident flux on boundary
ig	ignition
<i>i</i>	gaseous species
g	gas phase
m	moisture
<sup>1161</sup> net	net quantity
o	outward flux at boundary or observed value
r	radiative
s	solid (vegetative) fuel
v	virgin dry vegetation
F	fuel species
LES	value used in large eddy simulation
O <sub>2</sub>	oxygen species
$\lambda$	spectral dependence

Superscripts

<sup>1162</sup> /	derivative with respect to mixture fraction, $( )' = d( )/dZ$
T	transpose

Table 1: Thermophysical properties required in model and values used in base case simulations. Properties that were not measured in the two experimental field studies F19 or C064 are denoted by a hyphen (-). Values of these unknown properties in the simulation were either assumed or representative values were obtained from the literature sources cited.

	symbol, units	value used	F19	C064	other source (if needed)
gas phase	$\Delta h_c$ , kJ kg $^{-1}$	15600	-	-	grass (Susott 1982; Hough 1969) <sup>a</sup>
	$\chi_r$	0.35	-	-	wood cribs (Quintiere 1997) <sup>a</sup>
	$\chi_s$	0.02	-	-	Douglas fir (Bankston et al. 1981) <sup>a</sup>
	$dT_a/dz$ , C m $^{-1}$	0.0	-	-	assumed
	$U_2$ , m s $^{-1}$	experimental	4.8	4.6	
	$T_{g,a}$ , C	experimental	34	32	
solid phase	$\sigma_s$ , m $^{-1}$	experimental	12240	9770	
	$\chi_{\text{char}}$	0.2	-	-	grass (Susott 1982) <sup>a</sup>
	$c_{p,v}$ , kJ kg $^{-1}$ C $^{-1}$	varies with $T_s$	-	-	= 1.11 + 0.0037 $T_s$ (Parker 1989)
	$c_{p,m}$ , kJ kg $^{-1}$ C $^{-1}$	4.22	-	-	Incropera and Dewitt (1996)
	$h_s$ , m	experimental	0.51	0.21	
	$\rho_s$ , kg m $^{-3}$	512	-	-	grass (Rothermel 1972)
	$w_s$ , kg m $^{-2}$	experimental	0.313	0.283	
	$\beta_s$	experimental	0.0012	0.0026	
	$M$ %	experimental	5.8	6.3	
	$\Delta H_p$ kJ kg $^{-1}$	416	-	-	see discussion in Sec. A.2
	$T_{s,a}$ , C	$T_{g,a}$	-	-	assumed

<sup>a</sup>representative value from range of values found in the cited reference

Table 2: Simulation parameters for production runs. The horizontal grid cell sizes are equal  $\Delta x = \Delta y$ . The values of  $\Delta x$  given in the Table are for a  $300 \text{ m} \times 300 \text{ m}$  region in the center of the overall simulation domain. Outside this central region the horizontal grid cells are twice this size. The vertical grid size increases upward (72 grid cells are used). Each simulation required sixteen million grid cells and 11 processors. Case F19 required 44 cpu hours for 100 s of simulated time. Case C064 required 25 cpu hours for 100 s of simulated time. Case C064 required less resources because the overall heat release rate was approximately half that of case F19, resulting in smaller buoyancy induced velocities and, therefore, larger time steps.

simulation	$u_2, \text{ m s}^{-1}$	$L_{ig}, \text{m}$ — $d_{ig}, \text{ m}$	fuel bed	grass plot $x, y$ extent, m, m	sim. domain ex- tent, km — $\Delta x; \Delta z, \text{ m}$
head spread	1, 3, 4, 5	8, 25, 50, 100 — 6.7, 6.7, 3.3, 3.3	= exp F19	$200 \times 200$	$1.5 \times 1.5 \times 0.2$ — 1.6; 1.4 → 5.5
exp F19	4.9	175 — 3.3	see Table 1	$200 \times 200$	$1.5 \times 1.5 \times 0.2$ — 1.6; 1.4 → 5.5
exp C064	4.6	50 — 1.6	see Table 1	$104 \times 108$	$1.5 \times 1.5 \times 0.08$ — 1.6; 0.6 → 5.5

## Figures

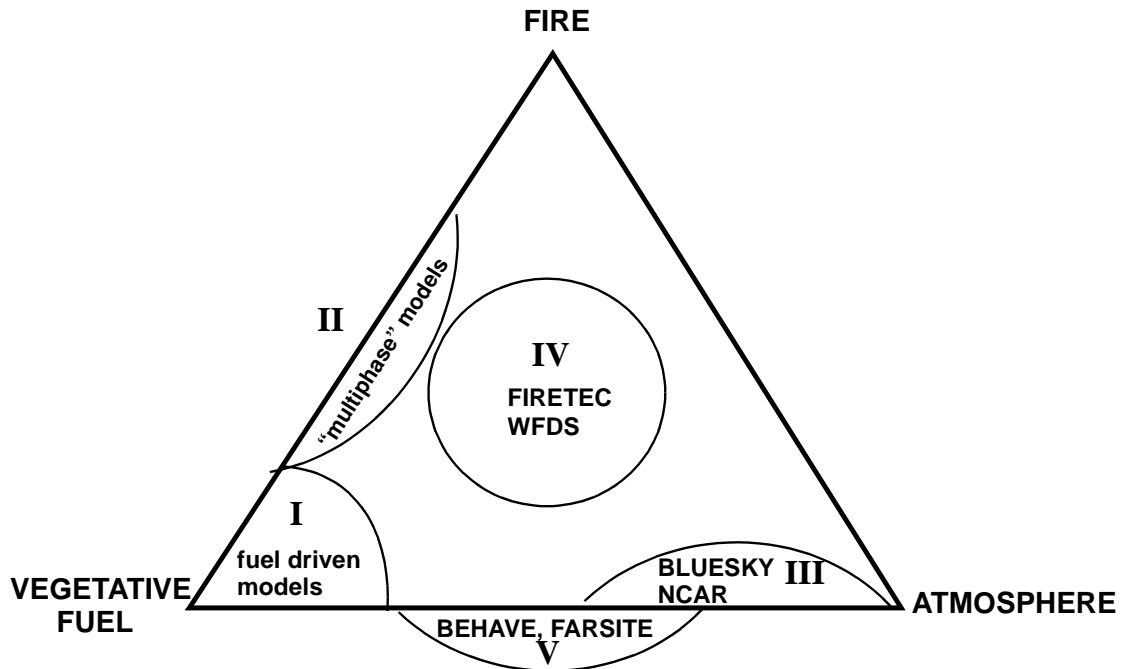
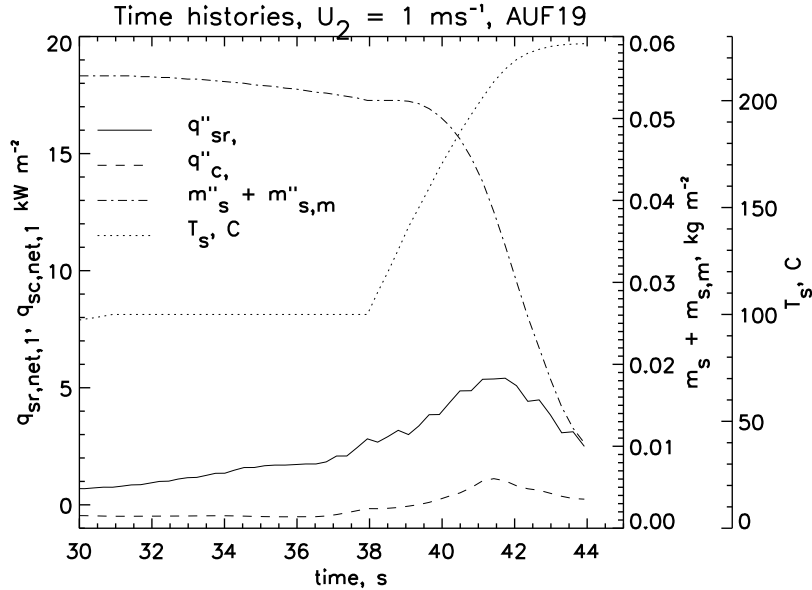
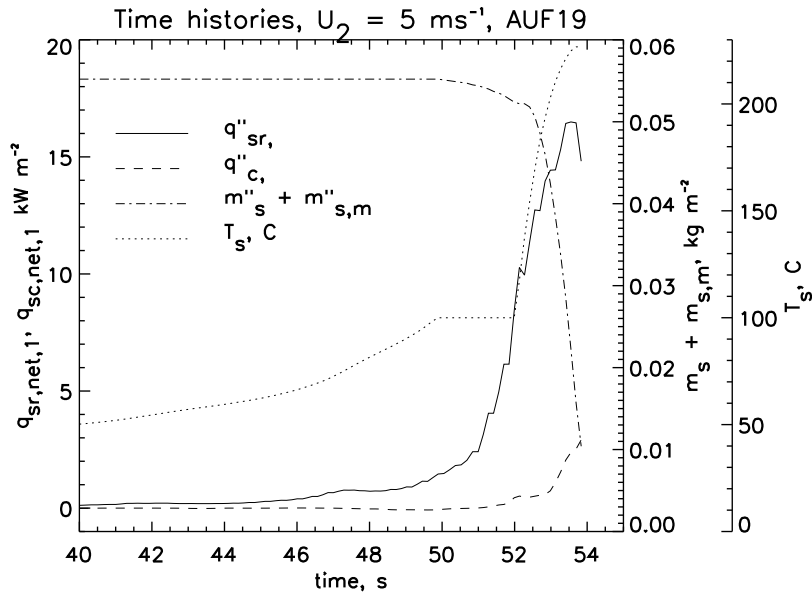


Figure 1: A schematic showing the relationship of different wildland fire models. Each approach is located according to its emphasis on the atmosphere, vegetative fuel, and/or fire component(s) of the working model. See text for a discussion of the figure.

1165



(a)



(b)

Figure 2: Time history of quantities in the uppermost layer of the grassland fuel model for two different ambient wind speeds at 2 m above ground;  $U_2 = 1 \text{ m s}^{-1}$  in Fig. (a) and  $U_2 = 5 \text{ m s}^{-1}$  in Fig. (b). In each figure the following are plotted: the convective ( $\dot{q}''_c$ ) and net radiative ( $\dot{q}''_{\text{sr}}$ ) fluxes on the top of the layer and the temperature and net mass loading (dry and moisture mass,  $m''_s + m''_{s,m}$ ) of the layer.

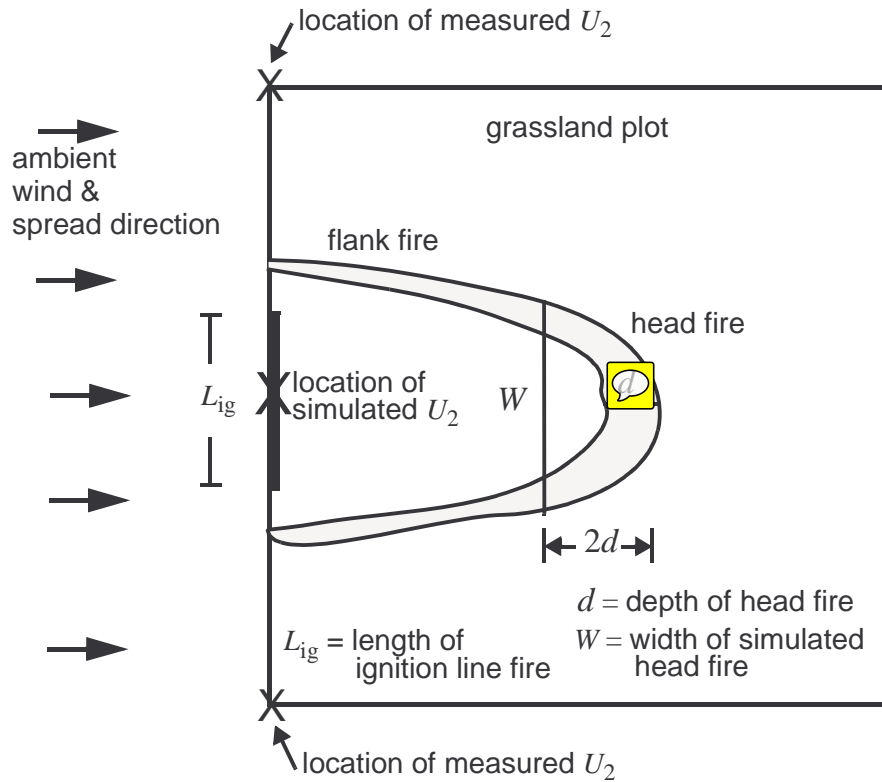
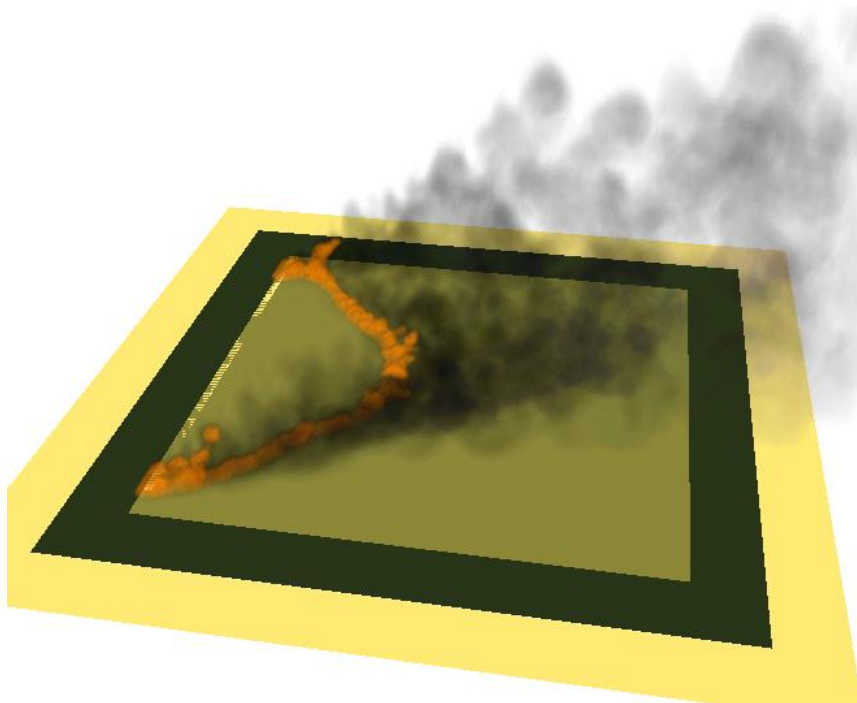


Figure 3: A schematic of a grassland fire. The ambient wind flows from left to right. The value of the wind speed,  $U_2$ , in the experiments is obtained by averaging the magnitude of the horizontal velocity measured at a height of  $z = 2$  m positioned at the upper and lower left-hand-side corners of the grassland plot. The value of the wind speed in the simulation is obtained from the computed component of the velocity vector parallel to the ambient wind at a height of  $z \approx 2$  m positioned above the center of the ignition line fire.

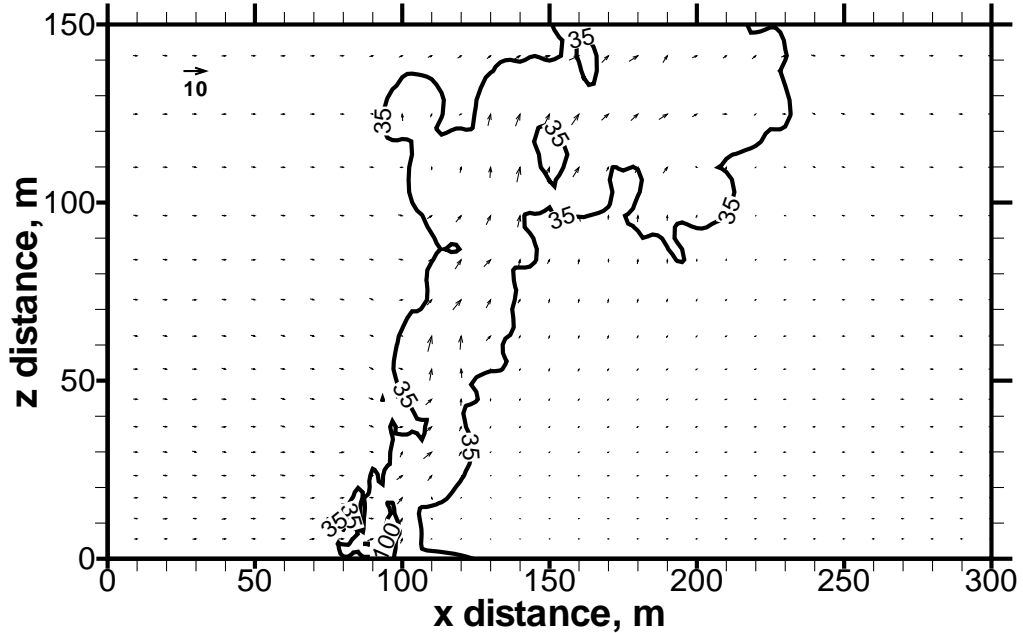


(a)

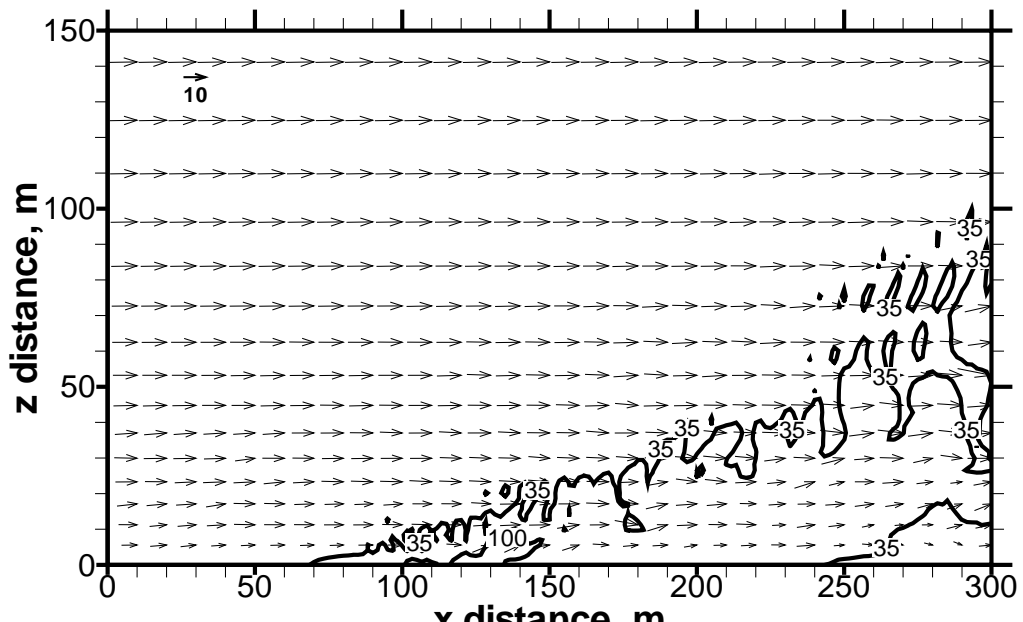


(b)

Figure 4: (a) Photograph of experimental fire F19 at  $t = 56$  s. (b) Snapshot of WFDS simulation of experimental fire F19 at  $t = 56$  s.



(a)



(b)

Figure 5: Temperature contours ( $35^{\circ}\text{C}$  and  $100^{\circ}\text{C}$ ) and velocity vectors in a  $x$ - $z$  plane for fires spreading in a grassland fuel bed with the characteristics of experiment F19 (see Table 1). The length of the ignition line fire was  $L_{\text{ig}} = 50 \text{ m}$ . The two figures correspond to two different wind speeds: (a)  $U_2 = 1 \text{ m s}^{-1}$  at  $t = 100 \text{ s}$ ; (b)  $U_2 = 5 \text{ m s}^{-1}$  at  $t = 50 \text{ s}$ . Horizontal spacing of vectors is  $10 \text{ m}$  (every sixth grid cell); vertical spacing varies because grid is stretched (every fourth cell is shown). The depth of the ignition line fire is approximately  $7 \text{ m}$  and is located at  $x = 50 \text{ m}$  to  $57 \text{ m}$ .

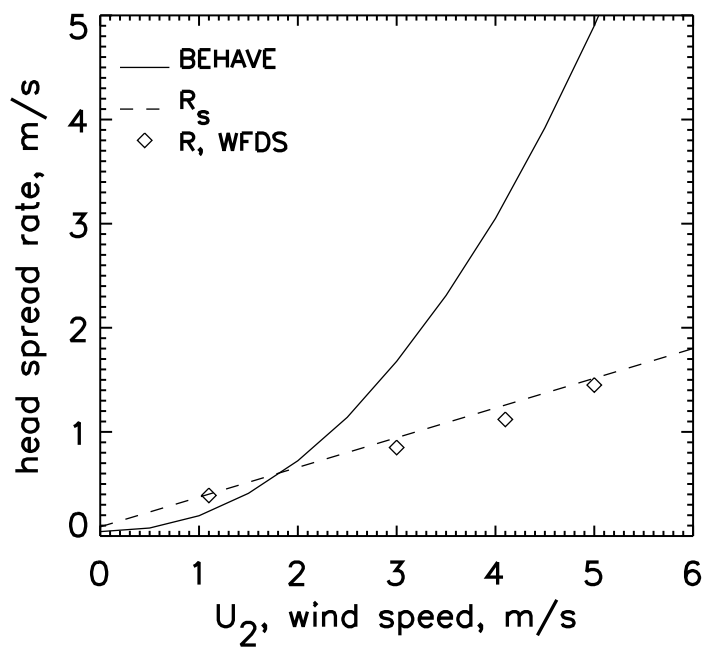


Figure 6: Spread rate of head fire versus the wind speed at a height of 2 m. Symbols are WFDS; solid line denoted BEHAVE is from the BehavePlus computer; program developed by the USDA Forest Service, and dashed line is the empirical expression, Eq. 3, from the grassland fire experiments (i.e., Eq. (4) in Cheney et al. (1998) with  $W \rightarrow \infty$ ).

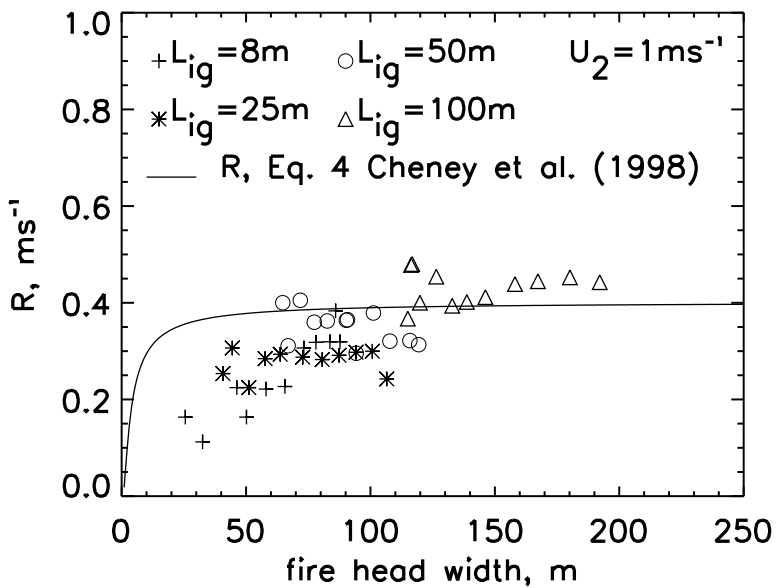


Figure 7: Spread rate of head fire versus the width of the head fire. The wind speed is  $U_2 = 1 \text{ m s}^{-1}$ . Spread rates from four different lengths of the ignition line fire ( $L_{\text{ig}} = 8 \text{ m}, 25 \text{ m}, 50 \text{ m}, 100 \text{ m}$ ) are shown. Symbols are WFDS; solid line is determined using the empirical expression, Eq. (2), from the grassland fire experiments (Eq. (4) in Cheney et al. (1998)).

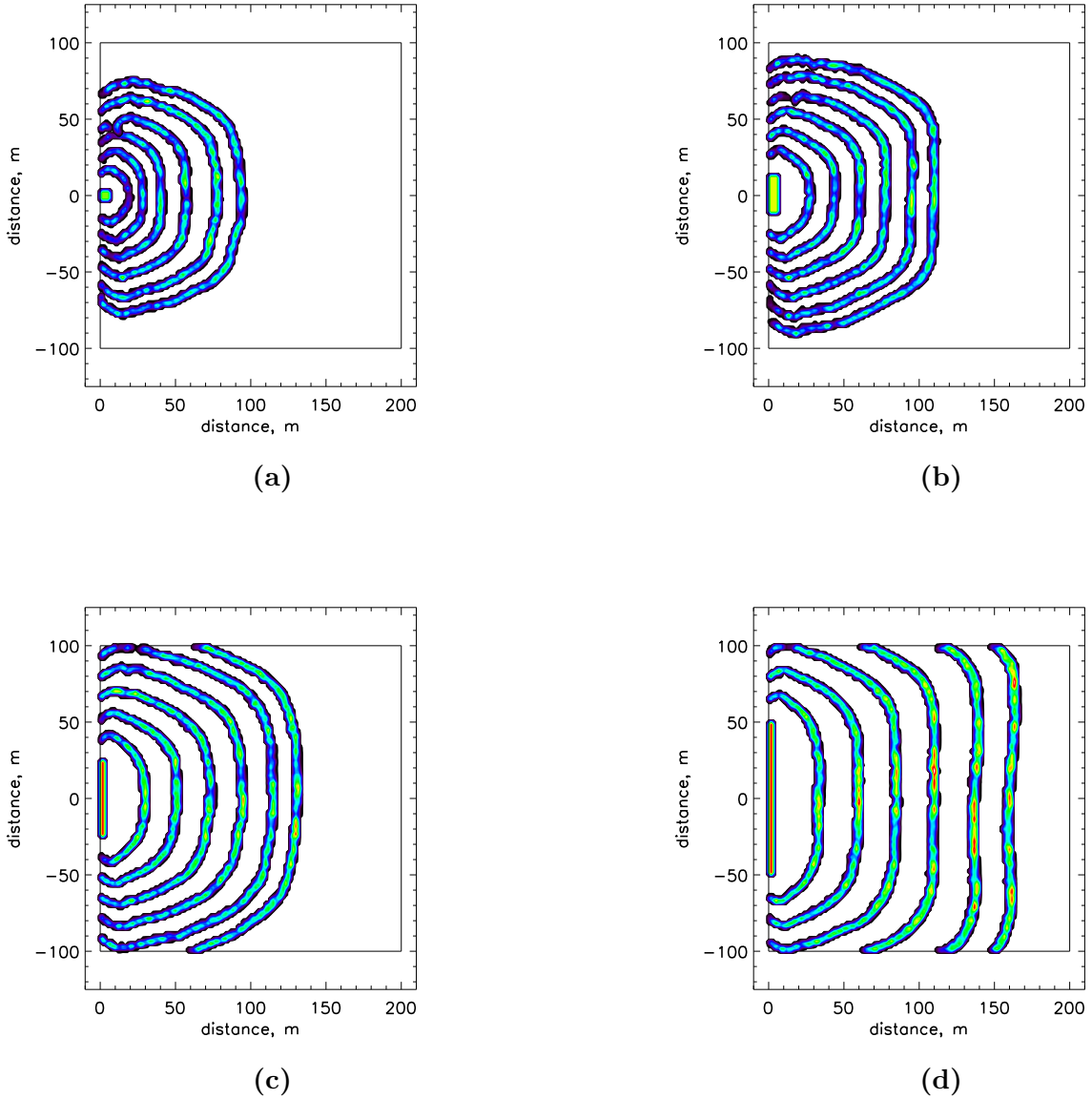


Figure 8: Time evolution of fire perimeters, shown as shaded contours of the mass loss rate, for  $U_2 = 1 \text{ m s}^{-1}$  and four different ignition line lengths  $L_{\text{ig}} = 8 \text{ m}, 25 \text{ m}, 50 \text{ m}, 100 \text{ m}$  in Fig. (a), (b), (c) and (d) respectively. The fire perimeters are plotted at times  $t = 0 \text{ s}, 60 \text{ s}, 120 \text{ s}, 180 \text{ s}, 240 \text{ s}, 300 \text{ s}$  and  $350 \text{ s}$ . The fire spreads in a  $200 \text{ m} \times 200 \text{ m}$  grassland plot with the fuel properties of experiment F19 listed in Table 1

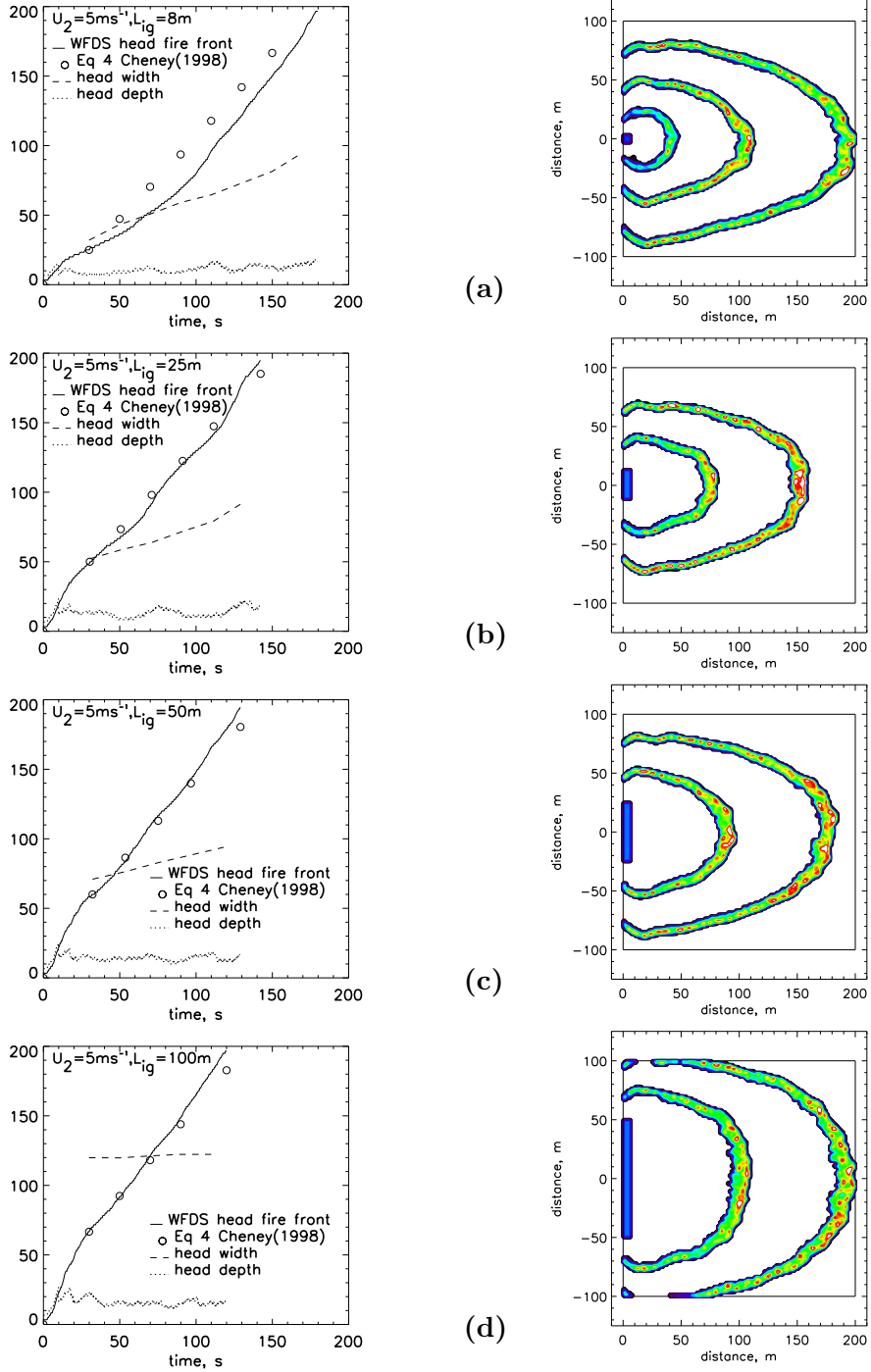


Figure 9: Left column shows the location of the leading edge of the head fire versus time from WFDS (solid line) and from using Eq. 2 (circles), an empirical formula for the quasi-steady spread. The wind speed is  $U_2 = 5 \text{ m s}^{-1}$  and the four ignition line fires are used,  $L_{\text{ig}} = 8 \text{ m}$  (a),  $25 \text{ m}$  (b),  $50 \text{ m}$  (c), and  $100 \text{ m}$  (d) long (same  $L_{\text{ig}}$  as in Fig. 8). The width (dashed line) and depth (dotted line) of the head fire are also plotted. The fire perimeter (shaded contours of mass loss rate) for each case are shown in the right column at 60 s intervals, starting at 0 s. The fire spreads in a  $200 \text{ m} \times 200 \text{ m}$  grassland plot with the fuel properties of experiment F19 listed in Table 1.

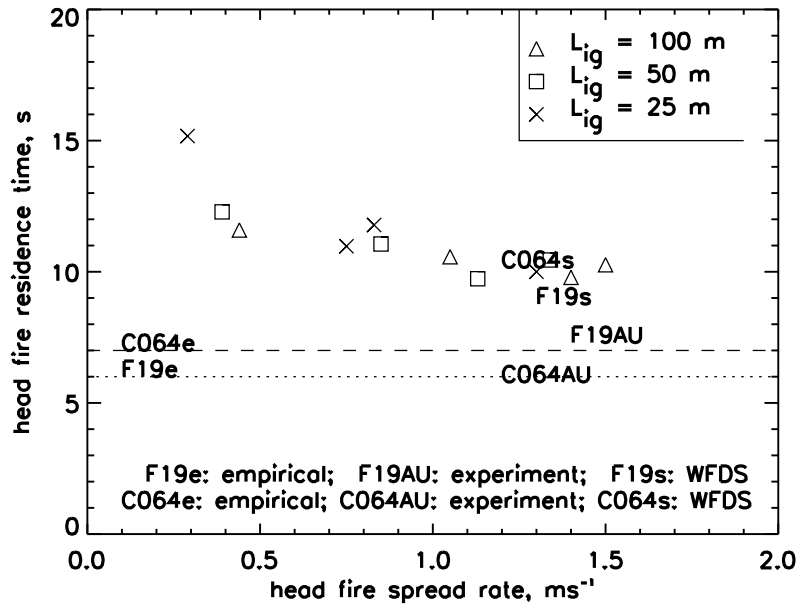


Figure 10: Residence time,  $\tau$  (s), from a number of sources. Symbols are  $\tau = dR^{-1}$  where  $d$  and  $R$  are determined from WFDS simulations with  $L_{ig} = 25$  m, 50 m, 100 m during quasi-steady flame spread in a fuel bed with the characteristics of the F19 experiments. The dotted line (labelled 'F19e') and dashed line (labelled 'C064e') are residence times from the empirical formula Eq. (4) using  $\sigma_s$  from experiment F19 and C064 (see Table 1), respectively. F19s and C064s are  $\tau = dR^{-1}$  values from WFDS simulations of experiments F19 and C064, respectively. F19AU and C064AU are  $\tau = dR^{-1}$  values from the experimentally measured  $d$  and  $R$ .

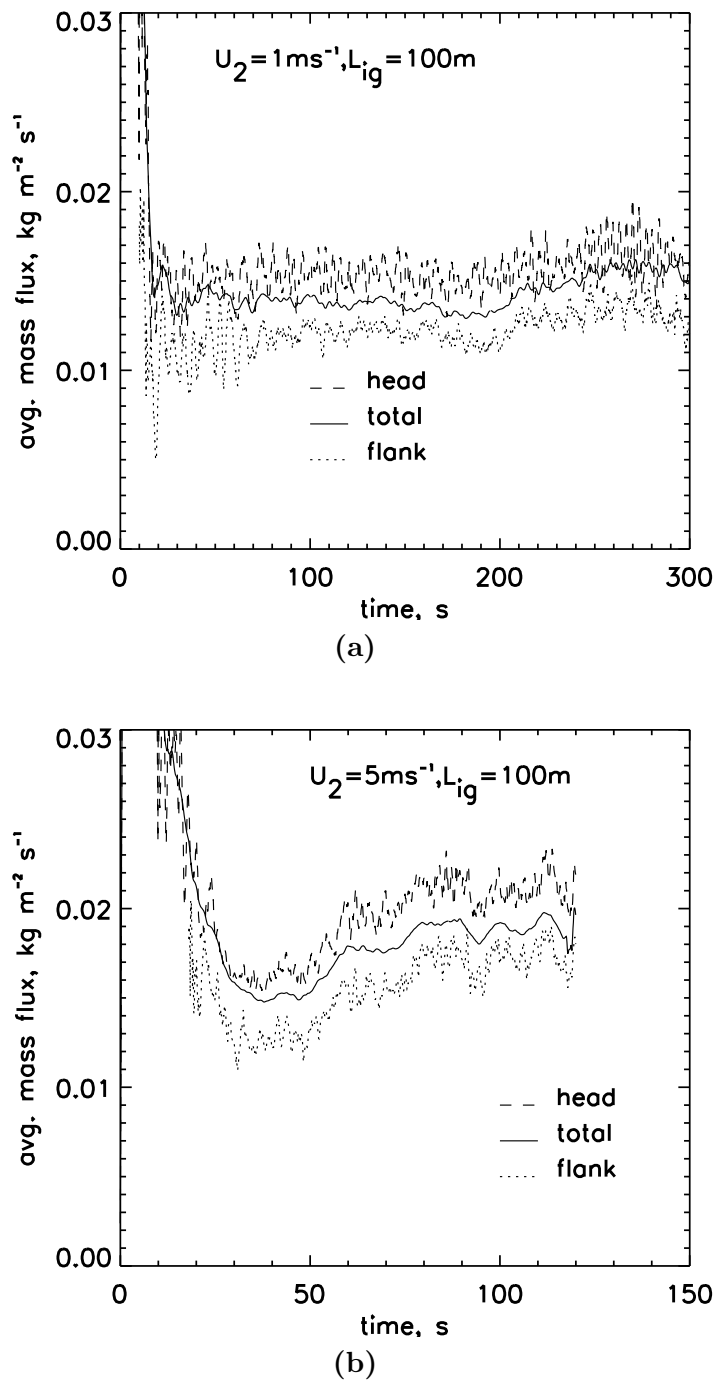
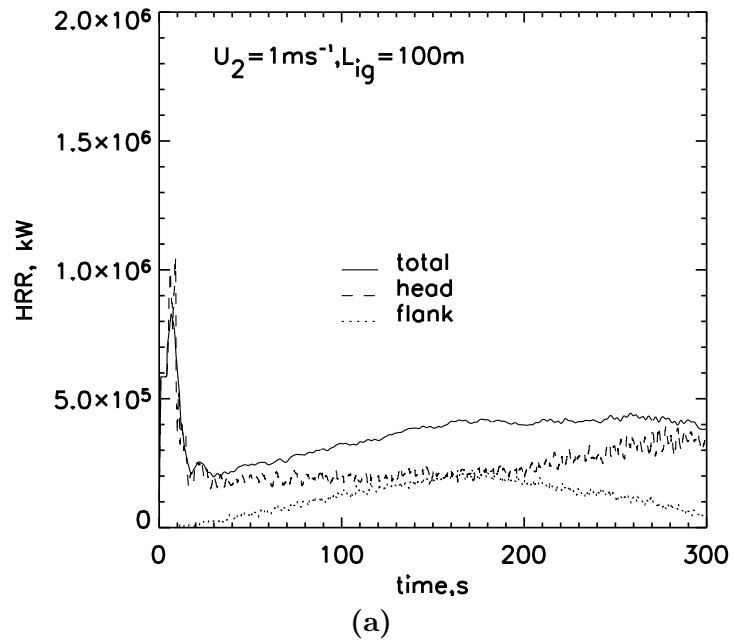
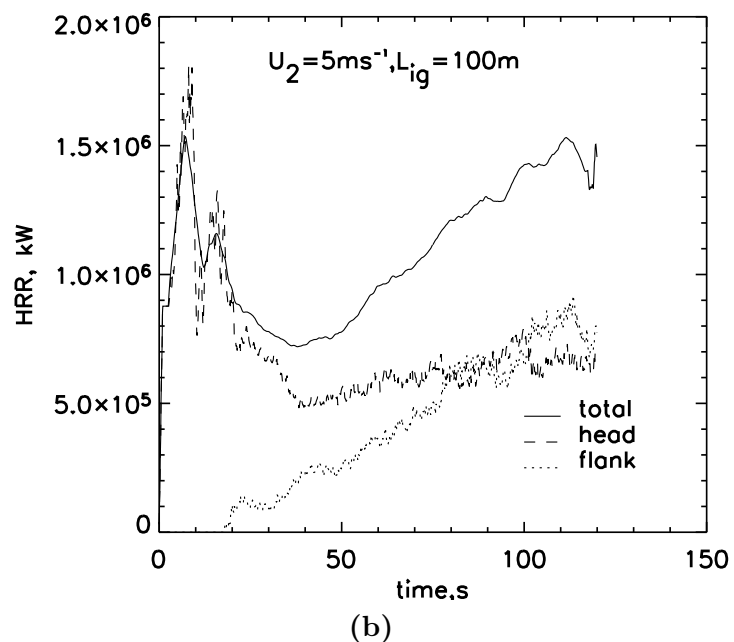


Figure 11: WFDS time histories of the mass flux of fuel gases during pyrolysis,  $\dot{m}_{s,pyr}''$  ( $\text{kg m}^{-2}\text{s}^{-1}$ ), averaged over the head fire, flank fires, and the total fire perimeter. In both figures  $L_{ig} = 100 \text{ m}$ . In both figures the fuel bed has the characteristics of the grass in AU experiment F19 (Table 1). In (a)  $U_2 = 1 \text{ m s}^{-1}$  and in (b)  $U_2 = 5 \text{ m s}^{-1}$ .

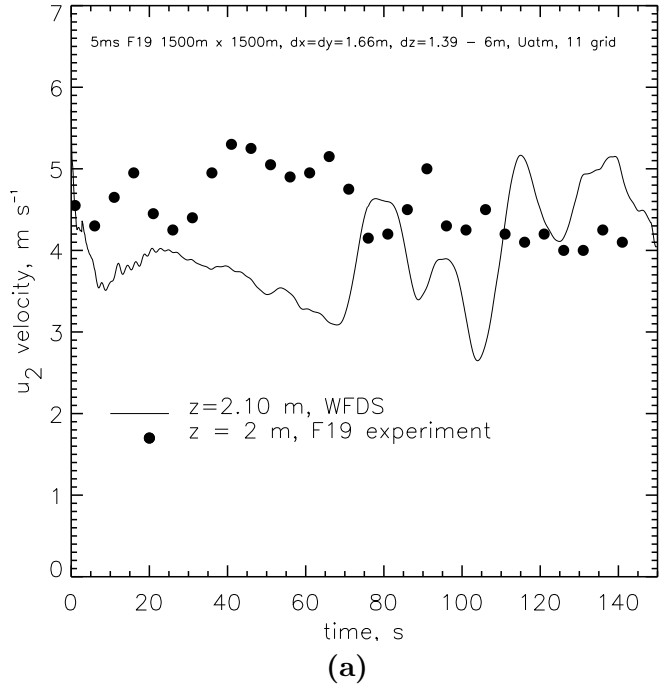


(a)

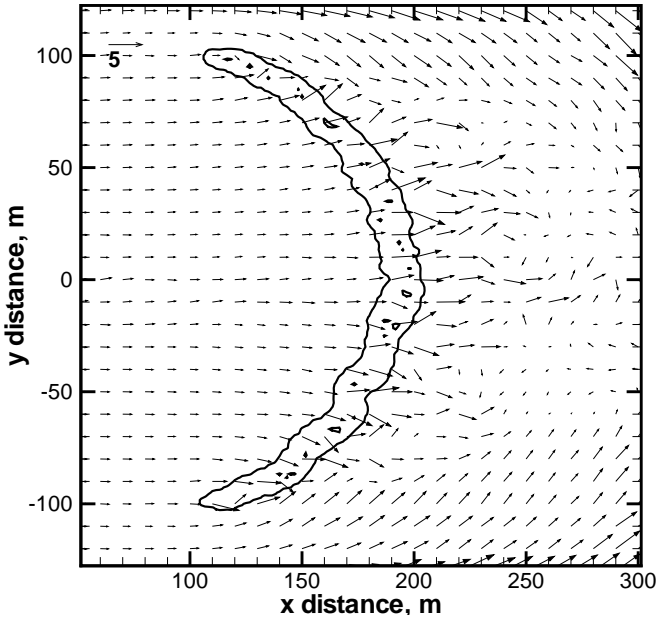


(b)

Figure 12: WFDS time histories of the heat release rate, HRR (kW), in the head fire, flank fires, and the total fire for the same cases shown in Fig. 11. In both figures  $L_{ig} = 100 \text{ m}$ . The fuel bed has the same characteristics as the grass in experiments F19 (Table 1). In (a)  $U_2 = 1 \text{ m s}^{-1}$  and in (b)  $U_2 = 5 \text{ m s}^{-1}$ .



(a)



(b)

Figure 13: WFDS and experimental results for experiment F19 at  $t = 100 \text{ s}$ . The ignition line fire was located at  $50 \text{ m} \leq x \leq 53.3 \text{ m}$ ,  $-86.7 \text{ m} \leq y \leq 86.7 \text{ m}$  (a) Time history of  $U_2$ . WFDS predictions after over 5 s (solid line) are located at a height of  $z = 2.1 \text{ m}$  above the midpoint of the ignition line (point  $x = 50, y = 0$  in figure (b)). Field measurements (filled circles) are the average of measurements taken every 5 s at  $z = 2 \text{ m}$  at the upwind corners of the  $200 \text{ m} \times 200 \text{ m}$  grassland plot ( $x = 50 \text{ m}, y = -100 \text{ m}, 100 \text{ m}$  in figure (b)). (b) Velocity vectors at a height of  $2.1 \text{ m}$  from WFDS at time  $t = 100 \text{ s}$ . Contour of the heat release rate showing borders of flaming region in the same plane is also shown. The WFDS grassland plot is located at  $50 \text{ m} \leq x \leq 250 \text{ m}$ ,  $-100 \text{ m} \leq y \leq 100 \text{ m}$ .

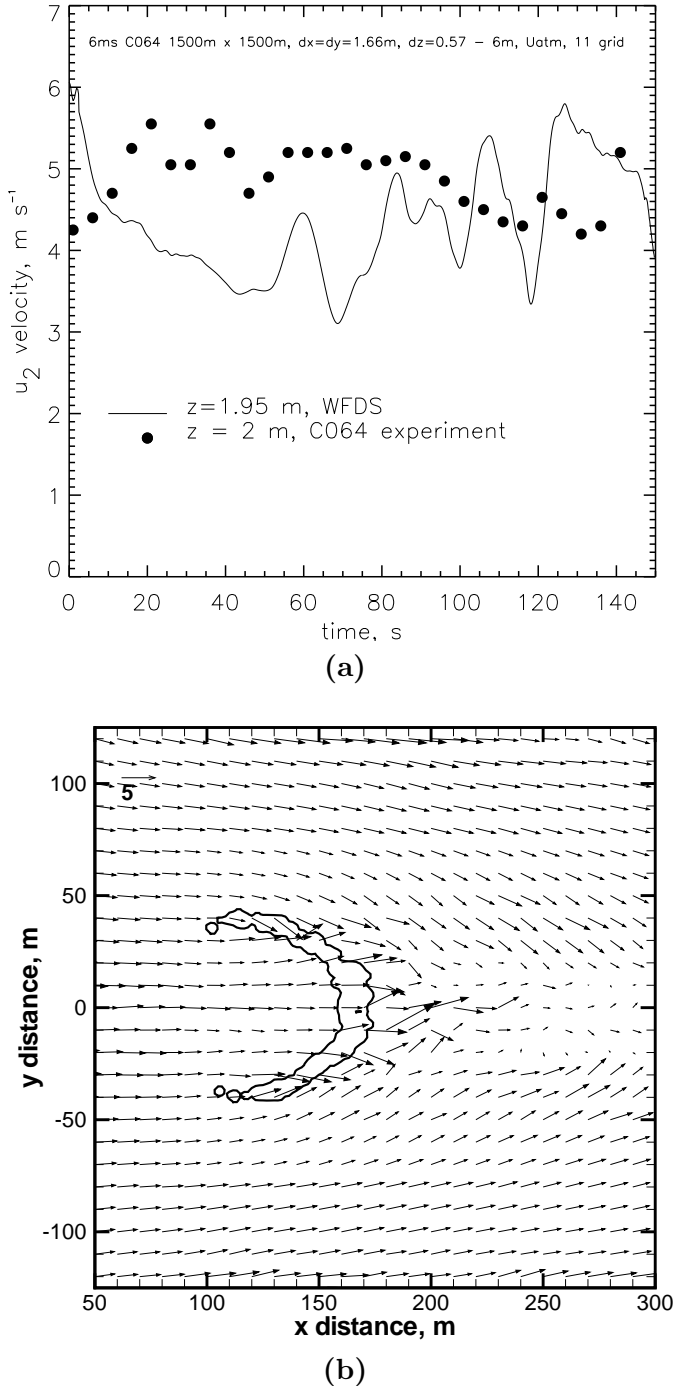
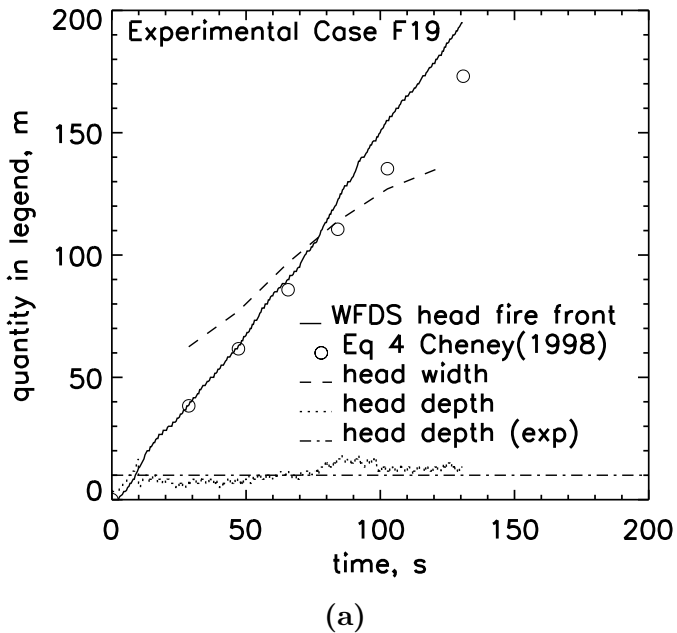
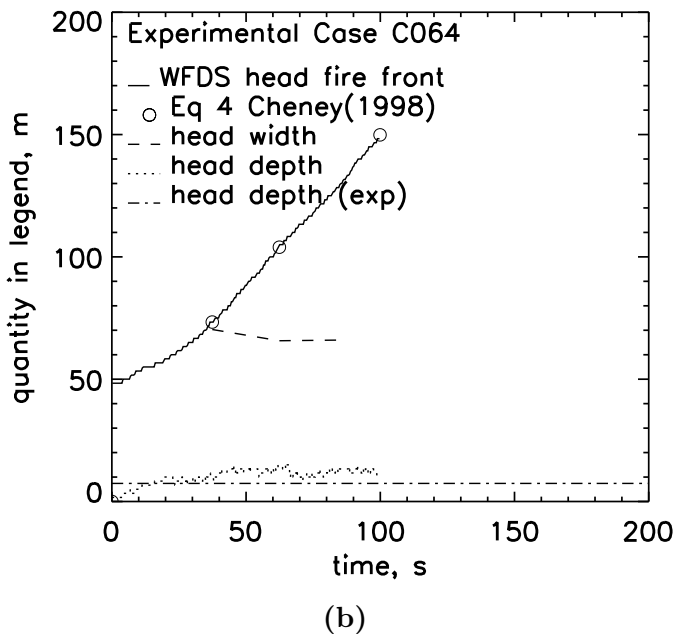


Figure 14: WFDS and experimental results for experiment C064 at  $t = 75$  s. The ignition line fire was at  $100 \text{ m} \leq x \leq 101.6 \text{ m}$ ,  $-25 \text{ m} \leq y \leq 25 \text{ m}$ . (a) Time history of  $U_2$ , the velocity 2 m above ground in the head fire spread direction. WFDS predictions average over 5 s (solid line) are located at a height of  $z = 1.95$  m above the midpoint of the ignition line (point  $x = 100$ ,  $y = 0$  in figure (b)). Field measurements (filled circles) are the average of measurements taken every 5 s at  $z = 1.95$  m at the upwind corners of the  $104 \text{ m} \times 108 \text{ m}$  grassland plot ( $x = 100$ ,  $y = -52, 52$  in figure (b)). (b) Velocity vectors at a height of  $1.95$  m from WFDS at time  $t = 100$  s. Contour of the heat release rate showing borders of flaming region in the same plane is also shown. The WFDS grassland plot is located at  $100 \text{ m} \leq x \leq 202 \text{ m}$ ,  $-53 \text{ m} \leq y \leq 53 \text{ m}$ .

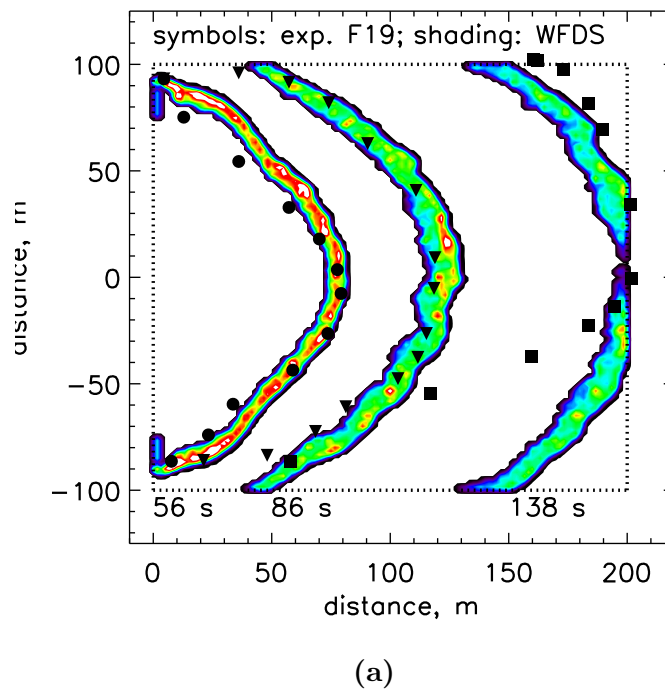


(a)

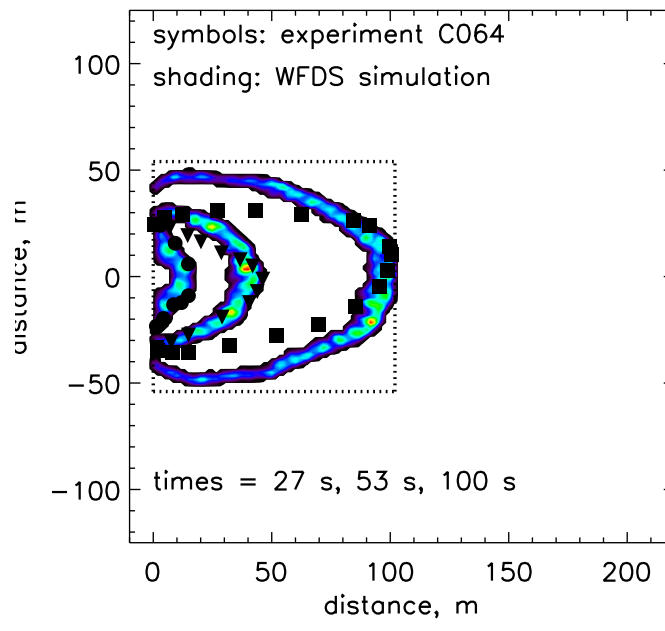


(b)

Figure 15: Time histories of the location of the leading edge, the width, and the depth of the head fire for experimental cases F19 and C064. The leading edge of the head fire from WFDS is shown as a solid line and as filled circles using the empirical spread rate formula, Eq. 2, with WFDS values for the head width,  $W$ . The head width from WFDS is a dashed line and the instantaneous depth a dotted line. The average head fire depth from field measurements is a dash-dot line.



(a)



(b)

Figure 16: Shaded contours show the actively burning fire bed (nonzero mass flux of gaseous fuel) from WFDS; symbols show the leading edge of the observed fire front in the experiments. The borders of the grassland plot are represented by the dashed line. (a) experiment F19 and (b) is experiment C064. See text for details and Table 1 for fuel/environmental parameters.

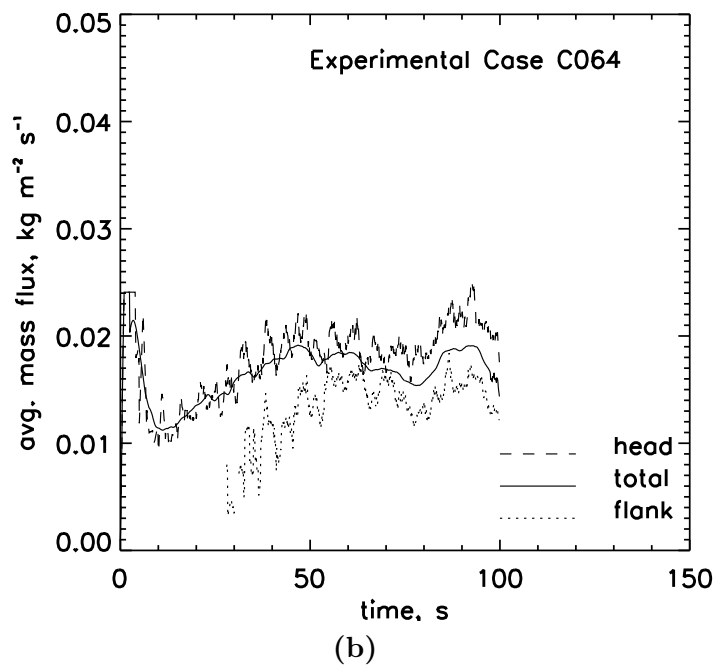
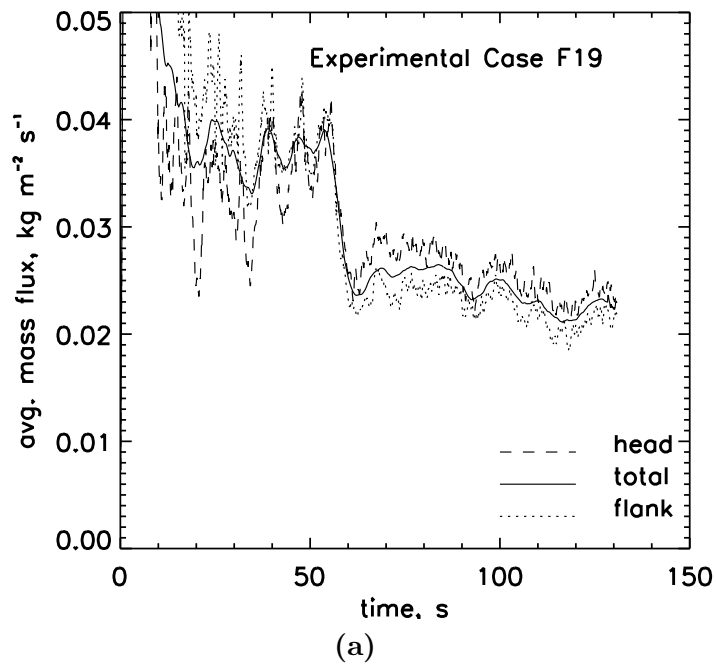


Figure 17: WFDS time histories, for experimental cases F19 and C064, of the mass flux of fuel gases during pyrolysis,  $\dot{m}_{s,\text{pyr}}''$  ( $\text{kg m}^{-2}\text{s}^{-1}$ ), averaged over the head fire, flank fires, and the total fire perimeter. In both figures  $L_{\text{ig}} = 100$  m. (a) is experimental case F19 and (b) is experimental case C064.

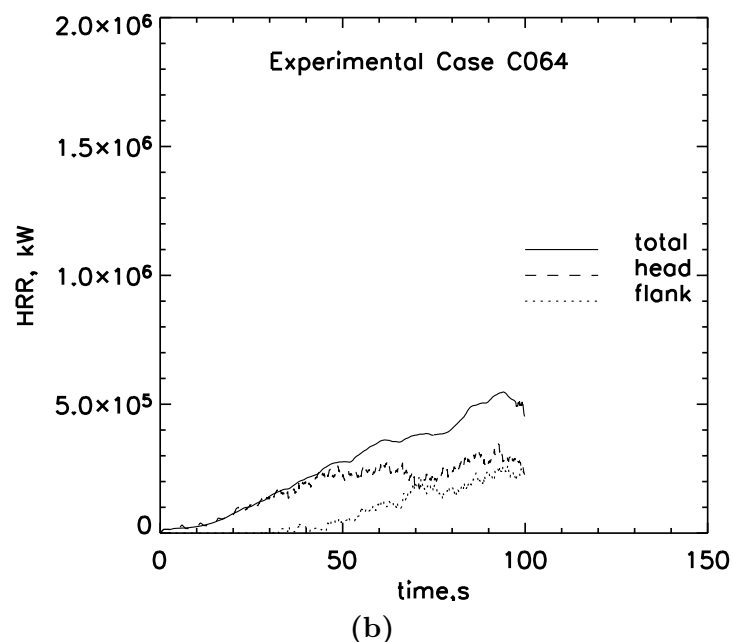
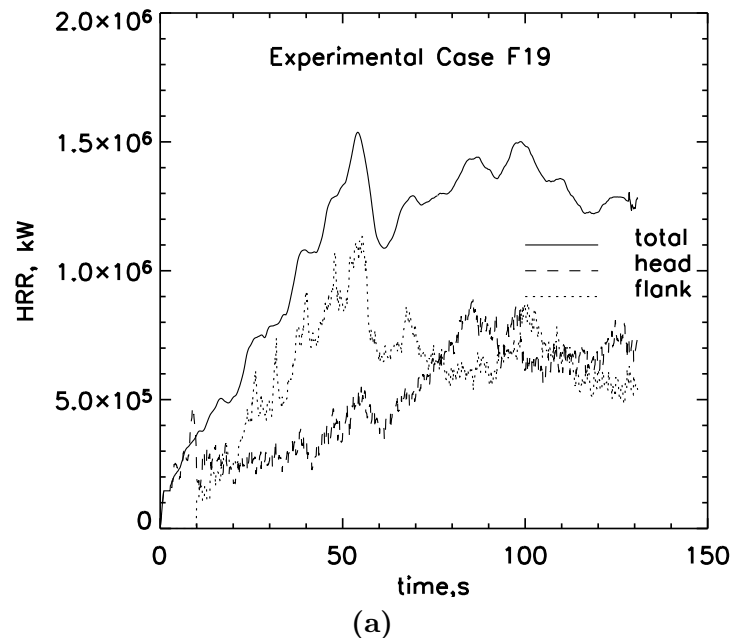
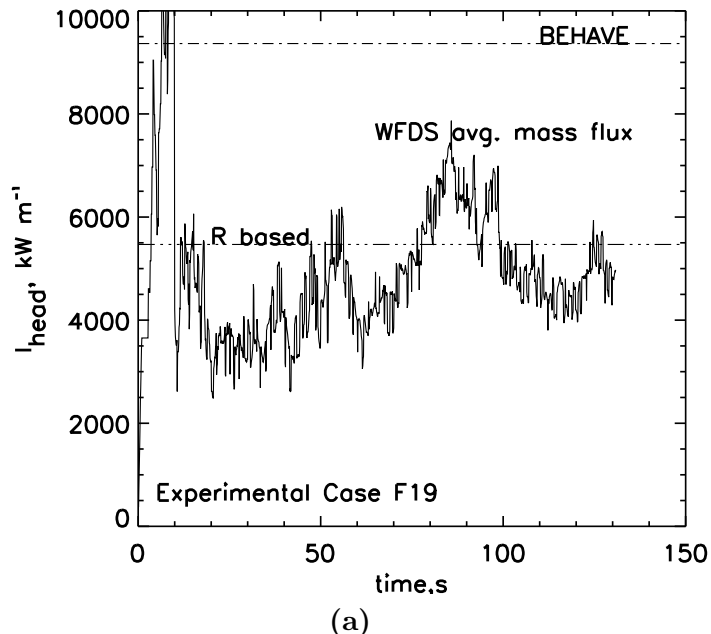
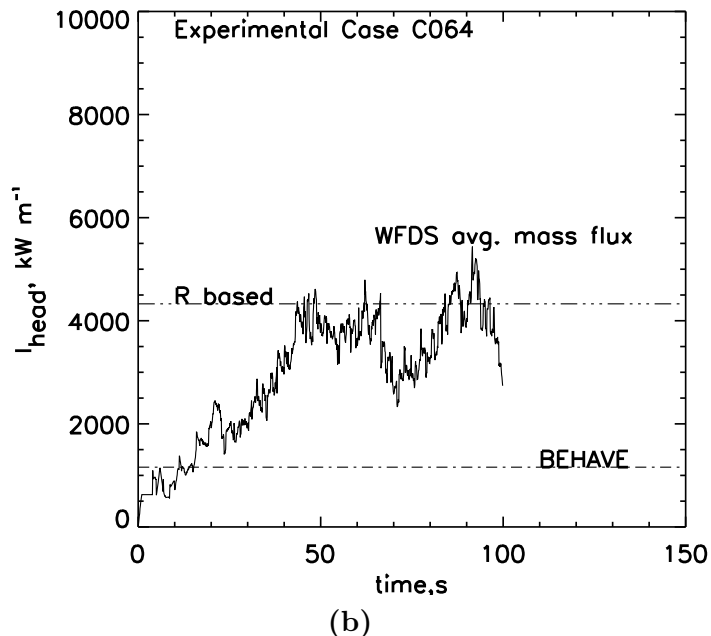


Figure 18: WFDS time histories, for experimental cases F19 and C064, of the heat release rate, HRR (kW), in the head fire, flank fires, and the total fire. (a) is experimental case F19 and (b) is experimental case C064.



(a)



(b)

Figure 19: Time history, for experimental cases F19 and C064, of the fire line intensity,  $I$  ( $\text{kW m}^{-1}$ ), in the head fire region of the fire perimeter. Solid line is from WFDS. The value of  $I$  from BehavePlus (line labelled 'BEHAVE') and from  $I = \Delta h_c(1 - \chi_{\text{char}})w_s R$  using the experimentally measured  $R$  (line labelled 'R based'; see Eq. (6)) are also shown. (a) is experimental case F19 and (b) is experimental case C064.

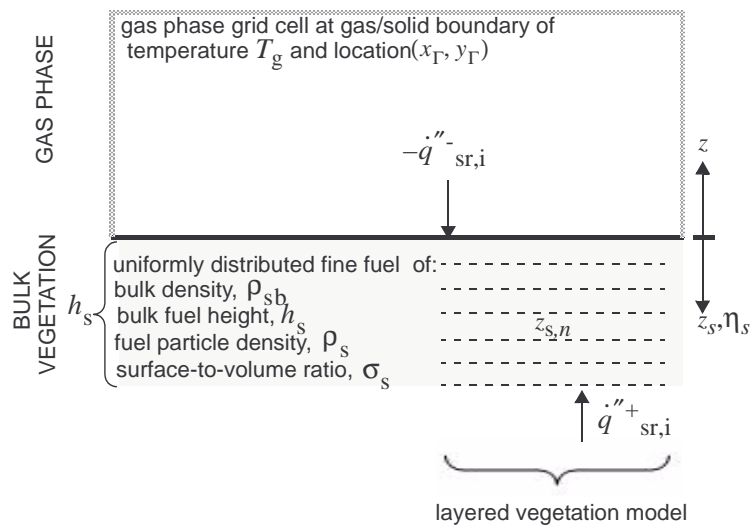


Figure 20: This figure summarizes the solid phase model. The vegetative fuel is characterized by its bulk density,  $\rho_{sb}$ , the fuel particle density,  $\rho_s$ , the surface-to-volume ratio of the fuel particles,  $\sigma_s$ , and the height of the bulk fuel,  $h_s$ . The fuel bed is divided into  $N_L$  layers and the evolution equations governing the heat up, drying, and pyrolysis of the vegetative fuel are solved within each layer as described in the text.